This is an Accepted Manuscript of a book chapter "The retina and the Stiles-Crawford effects" published by Routledge/CRC Press in Handbook of Visual Optics (Ed. P. Artal) Vol. I, 24 February 2017, available online: https://www.routledge.com/Handbook-of-Visual-Optics-Volume-One-Fundamentals-and-Eye-Optics/Artal/p/book/9780367869922"

CHAPTER 18:

The retina and the Stiles-Crawford effects

Brian Vohnsen, Advanced Optical Imaging Group, School of Physics, University College Dublin, Ireland

20.1 Retinal photoreceptor cones and rods

Refraction by the anterior eye is essential for proper focusing of light in the formation of images of the exterior world onto the retina. However, it is the absorption by pigments located within the photoreceptor cells that triggers the visual system. Understanding light-photoreceptor interactions is therefore necessary to unravel the complexities in the last optical step in the eye prior to subsequent neural responses. In the human retina there are two kinds of photoreceptors that are responsible for vision, *viz*., the rods and the cones. The rods are responsible for dim light (scotopic) vision whereas the cones are responsible for vision in normal and bright light (photopic) conditions. The transition from pure rod to cone-mediated vision is a combination of the two (mesoscopic) whereby the visual system has an astonishingly large dynamical range that spans about 12 log units most of which is accomplished by the retina as changes in pupil size accounts for little more than 1 log unit.

The visual pigment of the rods is rhodopsin whose peak of absorption is at a wavelength of approximately 496 nm whereas 3 different types of photopsin pigments are present in the cones categorized as S, M and L (short, medium and long wavelength) or blue, green and red

sensitive cones with broad absorption peaks centred at wavelengths of 419, 531, and 559 nm respectively [1] as seen in Fig. 20.1. The density of each type varies across the retina, and between individuals, but it is typically on the order of 5% S, 30% M and 65% L. In unbleached conditions each photoreceptor can absorb up to 2/3 of the incident light for wavelengths near its absorption peak and 2/3 of the absorbed photons will result in photoisomerization (cis $\rightarrow$ trans) of the visual pigment and thus a maximum catch efficiency of approximately 45% [2]. The absorption of a quantum of light triggers a biochemical cascade of events that results in a modified electrical current and associated photovoltage across the membrane wall which is communicated via bipolar cells to ganglion cells at the inner retina and further on via the optic nerve to the visual cortex.

The rod and cone photoreceptors are elongated cells with a length of close to 100μm (shorter in the parafovea) and in the healthy eye they are oriented with their central axis aligned towards a common point near the pupil centre [3]. Incident light reaches each photoreceptor at its synaptic end followed by the cell nucleus, the outer limiting membrane, the inner segment that contains high-refractive index mitochondria at the far end ellipsoid [4,5], before entering the outer segment that contains approximately 1000 layers of pigment and, if not absorbed or scattered, reaches the outer-segment termination beyond which a monolayer of retinal pigment epithelium (RPE) cells is located to absorb remnant light, nourish the outer segment, and provide phagocytic removal of cellular waste. The layered outer segments of rods consist of stacked lipid bilayer discs whereas for cones they consist of stacked membrane invaginations each of which contains thousands of pigment molecules [6] that are organized into an approximately square grid on each [7]. The pigment-containing discs and membranes are continuously renewed at a daily rate of approximately 10% with the oldest pigments being shredded at the outer segment terminations [8,9]. The fact that pigments are packed into the outer rather than the wider inner segments economizes

parafoveal photoreceptor metabolism by making more efficient use of pigments where visual acuity is lowest.

The total number of rods in the retina of a human eye equals approximately 120 million which is vastly superior to the approximately 6 million cones. Rods are absent at the fovea centralis but present in the spacing between cones at other eccentricities whereas the cones have their highest density in a hexagonal packing at the fovea reaching a peak value of approximately 160,000/mm^2 but falling off rapidly towards the parafovea with some 7,000 cones/mm^2 [10]. The outer segment length is largest for the foveal cones ~35μm and drops to approximately ~20μm for the parafoveal cones. The inner segment diameter of cones increases from approximately 2.2μm at the fovea to approximately 8.0μm at the parafovea whereas the outer segment is tapered down to approximately 2.0μm at the outer-segment termination. The diameter of rods is smallest being below 2.0μm. Fig. 20.2 shows histological images of rods and cones and a magnified view of outer segment membranes.

20.2 Introduction to the Stiles-Crawford effects and retinal directionality

The Stiles-Crawford effect refers commonly to the psychophysical observation reported by Walter. S. Stiles and Brian H. Crawford in 1933 that in photopic and mesoscopic conditions the eye is sensitive to the entrance point of light at the pupil [11]. When light enters the eye at an off-axis pupil point it is less efficient in triggering a visual sensation due to its oblique incidence on the retina [12]. This phenomenon is termed the Stiles-Crawford effect of the first kind (SCE-I). The reduction in visibility for obliquely incident light is described by a relative visibility, η, which is the ratio of subjectively-determined brightness for a ray of light that enters the eye at a given pupil point with respect to that of a parallel ray of light (for the unaccommodated emmetropic eye) that enters the eye at the pupil point of highest visibility located near the pupil centre though typically displaced nasally by approximately

0.5mm [13]. Thus, the SCE-I is described by the location of the pupil point of highest visibility and the corresponding distribution of the relative visibility across the pupil plane. This is normally expressed by a Gaussian function

$$\eta(r) = 10^{-\rho r^2} \qquad \text{Eq. (1)}$$

where ρ denotes the characteristic directionality parameter and *r* is the distance in the pupil plane from the point of highest visibility (if the distance is measured with respect to the geometrical pupil centre Eq. (1) is modified to $\eta(\boldsymbol{r}) = 10^{-\rho|\boldsymbol{r}-\boldsymbol{r}_0|^2}$ where $\boldsymbol{r}_0 = (x_0, y_0)$ denotes the location of the point of highest visibility and $\boldsymbol{r} = (x, y)$ denotes any point across the pupil). Eq. (1) was introduced by Stiles and Crawford using respectively a base-10 logarithm [14] and the natural base-*e* logarithm [15]. The value of the directionality parameter is lowest at the fovea (with a typical value of 0.05/mm^2) and increases with retinal eccentricity (to approximately 0.10/mm^2) although the accuracy of parafoveal SCE-I measurements is lower [16,17]. In general, the directionality might differ in the vertical and horizontal directions across the pupil (whereby the exponent in Eq. (1) is replaced using $\rho r^2 \rightarrow \rho_x x^2 + \rho_y y^2$) but observed differences are in general small [13] and rotational symmetry $\rho \equiv \rho_x \equiv \rho_y$ will for the most be used in the remainder of this chapter. Although the SCE-I was first discovered using white light it was soon repeated with narrow-bandwidth light which led to the discovery of a subtle wavelength dependence of the directionality parameter whereas the pupil location of the peak of visibility remains stable across the visible spectrum [12,14]. In scotopic conditions a psychophysical directionality is also present, though commonly neglected, as its impact is much smaller ($\rho \approx$ 0.01/mm^2) [18,19]. Measurement results for photopic and scotopic conditions of the SCE-I are shown in Fig. 20.3.

With the incident light power adjusted to compensate for the reduction in brightness caused by the SCE-I a minor change in colour appearance was first observed by Stiles [14]

and termed the Stiles-Crawford effect of the second kind (SCE-II) by Hansen [20]. The hue shift remains less understood than the SCE-I but the two effects are believed to share a common origin with the SCE-II containing additional information about the availability of visual pigments and the role of saturation.

Light which is backscattered from the retina displays also a directionality that is even more pronounced and has a spectral dependence that differs from its psychophysical counterpart. This effect is known as the optical Stiles-Crawford effect (OSCE) [21-25].

The fact that the SCE-I, SCE-II and OSCE share a common central pupil point with an associated directionality has led the present author to search for a unified model that will encapsulate the main characteristics of all three effects [26-28]. Measurement uncertainties, variations among subjects and the fact that different methodologies have been used are the main reasons why even today the origins of the Stiles-Crawford effects have still not been fully comprehended although significant insight has been gained. This was marked with a symposium in 2008 at the Frontiers in Optics conference commemorating “The Stiles-Crawford effects of the first and second kinds, 75 years of scientific achievements” and related publications summarize both the original discoveries and significant progress made [29,30] in the now more than 80 years since the discovery of the SCE-I.

That photoreceptors have directional properties has actually been known since 1844 when Brücke reported that these elongated cylindrical cells are endowed with an elevated refractive index and that their axes are aligned and point towards the eye pupil [31,32]. The pointing of cones is adaptable showing a kind of phototropism that has been demonstrated following cataract surgery and eye patching after which the point of highest visibility moves gradually towards the new pupil centre in the course of some 10 days [33,34]. Confocal microscopy imaging of frog retinas removed from the eye cup, but maintained in an isotonic liquid environment to maintain cellular activity (physiological environment), have confirmed

a remarkable reorientation of photoreceptor cells that adjust towards the incident rays so as to capture most light [35] although the underlying biomechanics involved remain little understood.

Already in 1843 Hannover had reported on detailed hexagonal microscopic patterns in individual photoreceptors of frog and fish retinas observed shortly after their death [36]. In 1961 Enoch provided experimental evidence of modal waveguide radiation patterns observed in transmission from single photoreceptors in isolated retinal tissues from primates including humans [37,38] examples of which are shown in Fig. 20.4. Packer *et al*. made microscopic photopigment density imaging using primate retinas before and after bleaching and found also a difference in optical path length of the rod and cone outer segment terminations [39]. It is important to keep in mind that all such observations are made only after having removed the retina from the eye which makes it prone to alterations at short time scales that may lead to modified optical properties and induce geometrical distortions when compared to those of the living retina in the intact eye. To overcome these limitations there is a great need for new methods that can accurately probe the photoreceptors in the living eye even at a subcellular level.

20.3 Methods used to examine the Stiles-Crawford effects

The SCE-I is typically analysed using a dual-path projection setup in which a reference light enters the eye at the pupil point of highest visibility and a separate test light enters the eye at sequentially different positions across the pupil either along a single horizontal cross section or in both horizontal and vertical traverses. The displacement of the test light is realized by rotation of a beam splitter [11,14] or a half-mirror mounted at the front focal plane of a lens used to generate a Maxwellian view [40] at its back focal plane [41,42], or by linear translation of the projected light source onto the pupil plane [13,43]. Computer control of

intensity and wavelength with liquid crystal filters [41,42] can speed up measurements although most time is required for the subjective determination of effective visibility at each entrance point. A uniaxial flickering system can minimize system errors caused by slight differences in dual-path systems such as minor spectral differences in the two paths [44]. Dilation of the eye pupil is required to approach an 8 mm pupil and a bite bar is typically used to minimize head motion during measurements. Both the reference and the test lights are observed in a Maxwellian view whereby the light enters the eye through a small pupil area to minimize the impact of ocular aberrations and to make it appear uniform within the field of view [40]. The apparent brightness of the reference field is then compared with the test field and one of them is adjusted in illumination power until a satisfactory match between the two has been accomplished, as judged by the subject, from which a measurement of the relative visibility can be made. Measurements are done monocularly (albeit binocular analysis has been attempted with one eye used for the test and the other eye used for the reference illumination [12]) using either a bipartite field where the test and reference fields are viewed simultaneously side-by-side extending typically 1 to 2 visual degrees or by letting the two fields overlap in space but flicker sequentially in time so that at any instant only the reference or the test is visible [11]. Minor variations of these methods exist in which the test and reference fields have different sizes or systems in which the viewer sees the reference field continuously onto which the test field is projected for incremental visibility determination.

It is vital that the size as well as the uniform appearance of both the test and reference fields remain stable throughout the experiment to avoid systematic errors in the visibility determination. Aberrations will tend to displace the test field when the entrance point is shifted across the pupil and therefore lower-order refractive errors are typically corrected using ophthalmic lenses [13], a Badal system [43] or current-driven tuneable lenses [42,44]. The two methods (bipartite and flicker) for SCE-I characterization are shown schematically

in Fig. 20.5. In either case, it is an enduring task to perform accurate measurements across the entire pupil without unintended movements of the eye for extended periods of time from minutes to hours, and thus only with highly collaborative subjects can accurate measurements be performed. To combat this, the characterization can be made objective by recording electroretinograms (ERG's) using different angles of incidence although the relation to the psychophysical SCE-I is nontrivial with signal contributions originating both from post-photoreceptor bipolar cells and from inner retinal neurons [45-47].

Rapid changes in the illumination direction can result in sudden brightness increases known as the transient Stiles-Crawford effect [48]. These can almost halve the apparent directionality when periodic flickering at 1 Hz is compared to that of 10 Hz (with the latter producing similar results to that of the conventional SCE-I) [44]. Following bleaching a change in directionality has also been observed once visual pigments recover from the intense illumination [49]. Even a sudden change in the direction of linear polarization of obliquely incident light can cause a change in apparent brightness by modified absorption [50]. These effects give insight into the temporal dynamics of the photoreceptor responses and the role of the spatial distribution of visual pigments.

How the SCE-I adds up across the pupil has been a central question already in the original work by Stiles and Crawford [11]. This question is pertinent to normal vision and pupil size using a Newtonian rather than a Maxwellian view since the angular spectrum of light at the retina differs in the two cases which may cause brightness [28] as well as colour differences [51]. From integration of Eq. (1) across a pupil diameter $d = 2R$, an effective pupil diameter d_{eff} ($< d$) can be derived as

$$d_{eff} = 2\sqrt{\frac{1-10^{-\rho R^2}}{\rho \ln(10)}} \qquad \text{Eq. (2)}$$

which approaches $1.32/\sqrt{\rho}$ for large pupils (and thus d_{eff} ~ 6mm for a directionality parameter $\rho = 0.05/\text{mm}^2$). Additivity has been found valid for normal pupil sizes using incoherent and partially coherent light, but for larger pupils differences appear due to blur even after correction of defocus [52-54]. Interestingly, this is not the case for highly coherent monochromatic laser light using annular pupils where light is symmetrically incident on the retina leading to complete cancellation of the SCE-I. In this case there is no wavefront slope across the resulting speckle pattern perceived by the photoreceptors as expressed by the Poynting vector of the light in the retinal plane [55-57]. The case of SCE-I characterization with coherent light is shown in Fig. 20.6.

Characterization of the SCE-II is performed using the same kind of experimental setting as for the SCE-I with the added complexity of an adjustable wavelength for the test to allow for better colour matching with the reference field [14,41] or, ideally, three separate adjustable sources with distinct wavelengths and brightness so that a complete colour match can be obtained [58]. The measurement is realized by first making a standard visibility match to compensate for the SCE-I and only thereafter to determine the best colour match to correct for the SCE-II.

Finally, characterization of the OSCE relies also on Maxwellian illumination to irradiate a bleached retinal area (which increases directionality and signal [59]) in order to capture an image of backscattered light with a camera that is located in a conjugate plane of the eye pupil [22,25] although a variant is possible where both the incident light and a closely-spaced small collection aperture are scanned in tandem across the eye pupil with light being captured point-by-point using a photomultiplier tube instead of a camera [60].

Imaging of the retina can be used to characterize the Stiles-Crawford effect both in terms of an average directionality with scanning laser ophthalmoscopy (SLO) [61] and optical coherence tomography (OCT) [62] and, when resolution allows it, at the level of single

photoreceptors [63,64]. In such measurements only the incoming light [63,64] or simultaneously both the incoming light and the collection aperture [61,62] are displaced across the eye pupil while capturing images with a brightness that is used for the analysis of directionality. It must be stressed that this objective method is not probing the visual response to oblique incidence but rather the directionality of light acceptance by and backscattering from the photoreceptors. When both the incident and the collected light is oblique the resulting effect may be viewed as a combination of the SCE-I and the OSCE with a resulting higher directionality [26]. Finally, the fact that the beam used in scanning retinal imaging technologies is being tightly focused onto the retina [61,62,64] may result in differences when compared to flood illumination of an extended retinal area [22,63] due to the match of illumination spot size to the photoreceptors being imaged [64].

20.4 Experimental results and subjective variations

Psychophysical analysis of SCE-I is a cumbersome process that requires not only accurate alignment and system calibration but also significant collaboration by the subject to minimize measurement errors. As a result, most studies have examined a very limited number of subjects although Applegate and Lakshminarayanan did report on monocular measurements with 670 nm red light and individual refractive corrections for 49 young subjects finding a directionality parameter in the range of $0.048/mm^2$ – $0.053/mm^2$ (horizontal, vertical) [13]. Fig. 20.7 shows SCE-I and SCE-II results obtained in the right eye of the author using a bipartite field at three distinct wavelengths. Each entrance point has been measured 4 times to determine average visibility and standard derivations for the SCE-I whereas the SCE-II results are based on 8 repeated measurements at each pupil entrance point.

Since photoreceptors point towards a common pupil point, eyes with a short axial length may have more inclined photoreceptors than eyes having large axial length as shown

schematically in Fig. 20.8. In developing eyes, growth mechanisms work towards maintaining emmetropization and in studies of myopia using chicks fitted with contact lenses altered eye growth can indeed be observed [65]. Relatedly, the SCE-I directionality and photoreceptor pointing might play a role for accommodation [66-68] although this remains somewhat an open question. In a study of highly myopes a 16% reduction in effective directionality was found [69] which agrees qualitatively well with the above argument. A simple geometrical analysis [42] suggests that directionality for the myopic eye, ρ_M, is reduced when compared to that of an emmetropic eye, ρ, as

$$\rho_M \approx (1+DL)^2 \rho \qquad \text{Eq. (3)}$$

where L is the effective axial length (length normalized by its refractive index) of an emmetropic eye (~17 mm) and the refractive error ($D < 0$) is expressed in dioptres. In turn, from Eq. (3) it is expected that hyperopic eyes ($D > 0$) have a higher directionality although this remains to be studied.

As a potential clinical tool the SCE-I, the SCE-II, and the OSCE have still not been fully explored. The retinal appearance of drusen, age-related macular degeneration [70], cone dystrophy [71], and retinitis pigmentosa [45,71] may all perturb photoreceptor alignment and thereby alter the Stiles-Crawford functions. Indeed, a reduced directionality and dislocated visibility peak locations in the pupil plane have been reported for patients using both psychophysical (SCE-I) and objective (OSCE) measures.

20.5 Optical models of the photoreceptor cones

Different models of photoreceptor-light interactions have been proposed based on principles that range from geometrical optics to electromagnetic wave propagation. For the most, models include only light in the forward direction as reflections are weak because of the low contrast of refractive indices across the photoreceptors. Nonetheless, objective methods and

retinal imaging relies on backscattered light and therefore some models have included reflections in the analysis.

20.5.1 Models of the SCE-I and the OSCE

It was clear from the outset that the SCE-I must originate in the retina as no other structure in the eye, or reflective differences at the cornea, could explain the significant reduction in visibility observed once an incident ray of light is displaced towards the pupil rim [11,12]. The first models of the SCE-I expanded on Brücke's description of the photoreceptor cell. Wright and Nelson followed by O'Brien argued that on account of total internal reflection light rays would be guided from the inner to the outer segment [12] and concentrated in the ellipsoid of each cone [72]. Multiple reflections in the ellipsoid could increase the angle of propagation and eventually lead to leakage. This would be most prominent for rays that enter the photoreceptor at an angle rather than along its cellular axis thereby mimicking the SCE-I before light reaches the pigments and stimulates vision by absorption in the outer segment. Rather than the angular dependence of light acceptance by single cones Safir and Hyams [73] suggested a smearing out in the acceptance angle, and thus a reduced directionality, as a collective effect caused by photoreceptor disarray. However, subsequent work has found no significant cone disarray near the fovea of the healthy retina [63].

Toraldo di Francia argued that on account of the small size of photoreceptors they should be considered as electromagnetic waveguides which would invalidate a purely geometrical approach [74]. Since then, waveguide models have taken sway not least due to the strong evidence of mode-like radiation patterns from photoreceptors as reported by Enoch [37,38]. Röhler and Fischer discussed waveguide modes and light absorption in photoreceptors [75] whereas Snyder and Pask introduced a complete cylindrical step-index

waveguide analysis of a single non-absorbing photoreceptor cone [76,77] that addressed directly the angular dependence of the SCE-I and has come to form the basis for much subsequent theoretical work. In doing so approximations have to be made regarding the exact geometrical shape and refractive index distribution across the photoreceptor and its surrounding medium, while the electromagnetic coupling between neighboring photoreceptors has typically been ignored despite of their tight cellular packing. The waveguide modes for a hexagonal arrangement of cylindrical waveguides representative of the cone photoreceptor mosaic has slow modes confined to each cylindrical waveguide (resembling the modes of an isolated waveguide) and faster modes confined to the space between the waveguides [78,79]. Accurate measurement of refractive indices in photoreceptors is challenging, and some variations exist in published values, but they generally find a higher refractive index of the outer than the inner segment [80]. Thus, the ellipsoid may be understood as a matching element between the two [74,81]. Waveguide characteristics are best described in terms of the characteristic *V*-number defined by

$$V = \frac{\pi d_w}{\lambda}\sqrt{n_1^2 - n_2^2} \quad . \qquad \text{Eq. (4)}$$

where n_1 is the refractive index of the waveguide core (inner or outer photoreceptor segment with diameter d_w) and n_2 is the lower refractive index of the surrounding medium. Reported refractive indices for the inner segment myoid are in the range 1.353 – 1.361 and in the outer segment 1.353 – 1.430 with the surrounding interstitial matrix having a refractive index of 1.340 (wavelength-dependent dispersion of these is typically omitted) [76,80]. When $V <$ 2.405 the waveguide becomes single mode (i.e., two orthogonal linear polarization modes with identical propagation constants) which is believed to be the case for foveal cones at least towards the long-wavelength end of the visible spectrum. Scalar optics can be used for ballistic light because of the small angles of propagation from the pupil to the retina (excluding intraocular scattering) and thus across any plane in the retina the forward-

propagating electromagnetic field, ψ_r, can be expressed as a sum of a discrete set of M guided modes, ψ_m, and a continuous set of radiative (nonguided) modes, ψ_{ng}:

$$\psi_r(\boldsymbol{r}) = \sum_{m=1}^{M} c_m \psi_m(\boldsymbol{r}) + \int_{-\infty}^{\infty}\int_{-\infty}^{\infty} c_{ng}(\boldsymbol{k}_\square)\psi_{ng}(\boldsymbol{r},\boldsymbol{k}_\square)d\boldsymbol{k}_\square \qquad \text{Eq. (5)}$$

where c_m and c_{ng} are scaling factors for each guided and nonguided mode, respectively, and $\boldsymbol{k}_\square$ is the in-plane wave-vector component (the integral limits will be effectively limited by the angular spectrum of the incident light). Due to the low refractive-index contrast of the photoreceptors and the surrounding matrix, linear-polarized modes (LP_{lm}) can be assumed which simplifies the calculations considerably [26]. It has been argued that once the light is guided the radiative components will have little impact on the absorption in the outer segments [82]. Absorption may be included in a waveguide model by use of a complex refractive index within the outer segment and possibly also in its surrounds. This results in leaking modes and for dim illumination it may modify the predictions considerable as more pigments would be available to absorb the light. Nonetheless, a reduced coupling for obliquely incident light is still seen that mimics the angular dependence of the SCE-I [83].

The fraction of incident light coupled to any waveguide can be calculated by the mode overlap integral across the entrance facet so that the total guided power (prior to absorption) in a waveguide is

$$P = \sum_{m=1}^{M} \left| \iint \psi_r \psi_m^* dxdy \right|^2 \quad . \qquad \text{Eq. (6)}$$

The angular dependence of coupled light power for a plane incident wave to different LP-modes of a cylindrical step-index waveguide is shown in Fig. 20.9.

The fundamental mode LP_{01} is almost identical to a Gaussian mode which is the fundamental mode of waveguides having a parabolically-graded index [26,84]. This is attractive from a mathematical point of view since it allows a number of analytical

derivations to be made including the analysis of tilt on the SCE-I, the matching of a focused beam to the waveguide, and the role of an off-axis incidence on the coupling efficiency. These examples are shown in Fig. 20.10. From the Gaussian mode an expression of the directionality parameter for a single-mode waveguide with a mode radius w (approximately equal to the waveguide core radius) can be found as

$$\rho = 2\log(e)\left(\frac{\pi n_{eye} w}{\lambda f_{eye}}\right)^2 \qquad \text{Eq. (7)}$$

for a schematic eye having focal length f_{eye} = 22.2mm and refractive index n_{eye} = 1.33. The factor of 2 in Eq. (7) appears when illuminated with a plane wave whereas if exposed to a Gaussian beam of light with a waist that is matched to the waveguide mode the factor of 2 cancels out. Eq. (7) shows a $1/\lambda^2$ wavelength dependence which agrees well with the dependence found from the OSCE [24]. The diameter dependence is in fair correspondence with the fact that parafoveal directionality (where the inner segment diameter and thus the mode radius is larger) is higher than at the fovea [16,17]. Although Eq. (7) has been derived for the incoming light the same holds true in the reverse situation of light diffracted from the waveguide and propagated towards the pupil. A numerical example with w = 1.0μm and λ = 0.55μm results in $\rho \sim 0.10/\text{mm}^2$ which is larger than the common SCE-I value at the fovea but similar to what has been measured for the OSCE [22,23].

As either the wavelength or the size of the analyzed photoreceptor waveguide is changed higher-order modes may appear that invalidate a simple Gaussian model. When the wavelength is modified it produces sudden variations of the directionality parameter once the number of allowed modes becomes altered. These variations smoothen across a retinal patch containing many photoreceptors with slightly different waveguide parameters whereby it resembles the spectral distribution of the directionality parameter first observed by Stiles [14]. The two are shown for comparison in Fig. 20.11. In the short-wavelength limit age-

dependent absorption in the crystalline lens contributes slightly to the effective directionality [85].

Detailed numerical electromagnetic finite-difference time-domain (FDTD) calculations in 2-D and 3-D for individual cylindrical waveguides representative of a single photoreceptor cone or rod have confirmed the angular dependence of light coupling [86] and also found a uniform spectral dependence [87] that gives added insight into the SCE-I and a plausible role for vision of the layered packing in the outer segments (although absorption was not included).

The drawbacks of any photoreceptor waveguide model are that the refractive indices are not fully known and that the shape of each cell (even the average cell) differs from that of the perfect cylindrical waveguide typically considered. Another concern is that their short length may prevent multiple reflections to occur when light is incident from normal pupil sizes being nearly parallel to the axis of each photoreceptor cell. This can severely limit the number of multiple reflections that may take place for the effective build-up of waveguide modes before possible absorption occurs. Moreover, for oblique incidence it is not clear what happens to the nonguided radiative modes that cannot contribute to vision as their inclusion would annul the directionality of the SCE-I. Thus, a waveguide model might oversimplify the actual interaction of light with visual pigments in normal non-bleaching illumination conditions unless both guided and radiative components of the light are fully accounted for. Enoch had stressed a similar concern prior to publishing his finding of transmission modes in bright light conditions of retinal tissue removed from the eye [88]. In the context of the OSCE a single aperture diffraction model has been used to model waveguiding from photoreceptors in conjunction with a rough surface model of the retina [23]. Backscattering of light from the choroid has also been used to describe the wavelength dependence of the

directionality parameter although this approach appears most appropriate in intense bleaching light where the likelihood of absorption is decreased [89].

The present author has taken a new approach to address the light gathering capabilities of outer segment pigment layers using optical reciprocity and antenna principles to argue for identical radiative lopes and collective acceptance angles of the photoreceptors [28]. Thus, the light acceptance angle by a single layer of dense pigments in an outer segment should correspond to the diffraction angles from an aperture with equal dimensions. Subdividing each layer into distinct light-induced point dipoles (representative of visual pigment molecules) allows light scattering and acceptance calculations to be made in any direction when assuming that all other refractive indices beyond the outer segment can be taken as equal (this is for simplicity rather than a fundamental limitation). Pigment molecules are densely packed on each layer [6,7] which makes them collectively have similar light-gathering capabilities as uniform layers. Thus, by stacking apertures to represent one or multiple outer segments it allows for modelling of their collective light acceptance. This approach ignores multiple scattering between layers [28] notwithstanding that it may produce resonant effects at specific wavelengths [87]. Light scattering between adjacent photoreceptors can easily be included and multiple scattering could potentially be included via a self-consistent set of equations that can account for coupled scattering between layers and neighbouring outer segments [28,90]. Optical reciprocity implies that the outer segment receives light in the same way that it would emit had it been the source of the light and the propagation direction reversed. This is true for the waveguide model of the retinal receptor and it is equally valid for a layered model of the outer segment. Therefore, such an approach is useful to determine the pupil field for light propagated from (or to) each layer in the outer segment.

This pupil field can be calculated using the standard Fraunhofer diffraction equation for single circular apertures each having the diameter d_w of the outer segment layer that it represents. For N parallel apertures spaced at a layer-to-layer distance of δ the diffracted fields in the pupil plane can be added resulting in

$$\psi_{pupil}(r) = \sum_{n=1}^{N} \frac{A_n n_{eye}}{i\lambda z_n} \exp\left(ik(z_n + \frac{r^2}{2z_n}) \right) \left(\frac{2J_1(krd_w / 2z_n)}{krd_w / 2z_n} \right) \qquad \text{Eq. (8)}$$

where J_1 is the first-order Bessel function of the first kind and the wavenumber is $k = 2\pi n_{eye} / \lambda$. The $z_n = f_{eye} + h + (n-1)\delta$ is the axial distance from aperture n to the pupil of the schematic eye and h is the distance from the first outer segment layer to the inner limiting membrane. The total length of the outer segment is $L = N(\delta - 1)$. Since all the apertures at different depths in the outer segment are driven by the same incident light this must be phase-locked at the pupil which is accomplished by connecting the amplitude factors between the layers using $A_{n+1} = A_n \exp(-ik\delta)$.

The straightforward addition from each layer in Eq. (8) is based on the assumption that all layers capture light independently. The electromagnetic wave is thus allowed to diffract beyond the cell boundaries of the photoreceptor and waveguiding is not enforced. The high refractive index of outer segments is due to the high density of pigments contained in the stacked membrane infoldings or discs. Dim light will be absorbed in a fraction of each outer segment and only intense light will propagate all the way to the outer segment terminations. Absorption can be introduced ad-hoc in the axial direction by use of Beer-Lambert's law in the amplitude factor A_n to exponentially dampen the impact of pigments located deep within the outer segment. Disarray of the layers in a single photoreceptor, or between adjacent photoreceptors, would still introduce a smearing out and reduction of the directionality. The layered diffraction model and resulting directionality curves (intensity at the pupil plane

$\left|\psi_{pupil}\right|^2$) for a schematic eye for dim and bright light, respectively, is shown in Fig. 20.12. In this model, the illumination brightness becomes a deciding factor as for dim light (absorbed in a fraction of the full outer segment length) directionality is low but in bright light conditions more pigment is bleached and the directionality parameter increases (due to the contribution from deeply located layers) thus giving a direct physical meaning to the role of bleaching for the SCE-I [91]. Thus the model does not only give directionality predictions for the SCE-I but also for the OSCE usually analysed in bleached conditions where contributions from the entire outer segment length will increase the effective directionality.

20.5.2 Models of the SCE-II

The SCE-II has most commonly been considered a result of self-screening by pigments and light leakage rather than waveguiding [11,92,93]. When oblique light traverses the retina, the distance through which it can interact with visual pigments is shortened as compared to on-axis incidence. This ray-optical approach seems somewhat at odds with the waveguide model. Independent of the exact mechanisms involved it is worth noting that most studies have made use of a finite bandwidth illumination and thus differences in visibility across the spectral band should be expected. To examine this further one may express the spectral sensitivity curve (luminous function) for the eye as $\eta_{\max}(\lambda)$, with the highest sensitivity equal to unity at a wavelength of 555 nm, whereby the SCE-I function from Eq. (1) can be modified into a spectrally-dependent "SCE-I colour visibility function" [27]

$$\eta(r,\lambda) = \eta_{\max}(\lambda)10^{-\rho(\lambda)r^2} \qquad \text{Eq. (9)}$$

where the wavelength dependencies of the effective visibility and directionality parameter have been made explicit. The wavelength derivative of this function is

$$\frac{\partial\eta(r,\lambda)}{\partial\lambda} = \left[\frac{d\eta_{\max}}{d\lambda} - \eta_{\max}\frac{d\rho}{d\lambda}r^2\ln(10)\right]10^{-\rho(\lambda)r^2} \quad . \qquad \text{Eq. (10)}$$

Any visibility difference across the spectral bandwidth of the illumination, $\Delta\lambda$, for a chosen central wavelength λ_0, would cause an incremental visibility difference (and thus a hue shift) equal to $\Delta\eta = \left.\frac{\partial\eta}{\partial\lambda}\right|_{\lambda_0} \Delta\lambda$. Analysis of the SCE-II consists of a subjective colour comparison between the test and reference fields that enter the eye pupil through pupil point $r = r_0$ and $r = 0$, respectively, and only after having compensated for the SCE-I by multiplying with $10^{\rho(\lambda_0)r_0^2}$ at the chosen wavelength. Eq. (10) can be rewritten to consider this comparative case resulting in

$$\begin{aligned}\Delta f &= \left(\left.\frac{\partial\eta(r,\lambda)}{\partial\lambda}\right|_{r=r_0} - \left.\frac{\partial\eta(r,\lambda)}{\partial\lambda}\right|_{r=0} \right) 10^{\rho(\lambda_0)r_0^2} \\ &= \frac{d\eta_{\max}}{d\lambda}\left(10^{-(\rho(\lambda)-\rho(\lambda_0))r_0^2} - 1\right) - \eta_{\max}\left(\frac{d\rho}{d\lambda} r_0^2 \ln(10)\right) 10^{-(\rho(\lambda)-\rho(\lambda_0))r_0^2}\end{aligned} \qquad \text{Eq. (11)}$$

which can be interpreted as a "SCE-II hue-shift function" per unit wavelength caused by a finite bandwidth and the spectrally nonuniform sensitivity curve and directionality parameter of the eye [27]. The incremental visibility is found by multiplying Eq. (11) with the spectral bandwidth $\Delta\lambda$. If the dispersion of the directionality parameter is partially ignored by setting $d\rho/d\lambda = 0$ (but kept in the exponent) Eq. (11) can be simplified to

$$\Delta f \approx \frac{d\eta_{\max}}{d\lambda}\left(10^{-(\rho(\lambda)-\rho(\lambda_0))r_0^2} - 1\right) \approx \frac{d\eta_{\max}}{d\lambda} \ln(10)\left(\rho(\lambda) - \rho(\lambda_0)\right) r_0^2 \quad . \qquad \text{Eq. (12)}$$

In this approximation, no hue shift should be expected at the spectral sensitivity peak of the eye where $d\eta_{\max}/d\lambda = 0$. In turn, the largest predicted hue shift (positive or negative) should occur at wavelengths that coincide with the largest slope of the spectral sensitivity curve of the eye shown in Fig. 20.1. Based on the CIE data the largest slope is at wavelengths of 510 nm and 605 nm, respectively, where the largest positive or negative hue shifts should therefore be expected.

Near to the pupil point of highest visibility (r = 0) the predicted hue shift has a parabolic dependence on the tested pupil point location r_0 centred at the peak of visibility and it may either cause a negative or a positive hue shift. At short wavelengths (below 555 nm) $d\eta_{\max}/d\lambda > 0$ for which the upper end of the spectral band dominates whereas at long wavelengths (above 555 nm) $d\eta_{\max}/d\lambda < 0$ and the lower end of the spectral band would dominate in the visual response. For any finite bandwidth the pre-compensation of the SCE-I will therefore be incomplete when analysing the SCE-II. The added complexity of the second term in Eq. (11) containing the spectral derivative of the directionality parameter complicates the analysis and may modify somewhat the predictions. Assuming the same spectral dependence as for the OSCE, i.e., $\rho \propto 1/\lambda^2$ then the derivative $d\rho/d\lambda < 0$ and the 2nd term in Eq. (11) will raise the sum of the terms. Eq. (9) and Eq. (11) are both shown in Fig. 20.13 that also highlights selected cross sections. As can be seen Δf is in qualitatively good agreement with reported SCE-II distributions both as a function of pupil point and as a function of wavelength [14,41]. It must be stressed that in this model entirely monochromatic (zero bandwidth) illumination produces no hue shift. Differences in the directionality parameter of different cone types could be included in the model (S-cones are slightly wider than M and L-cones and may therefore have a slightly higher directionality) as well as partial bleaching of S, M or L-cone pigments (modifying the initial 5%, 30% and 65% distribution) allowing apparent colour changes even for entirely monochromatic light.

20.6 Fitting functions for the Stiles-Crawford effects and the directionality parameter

It is often convenient to plot the logarithm of Eq. (1) rather than the Gaussian function of Stiles and Crawford [14,15] as this gives a parabolic dependence on pupil point, i.e., $\log(\eta) = -\rho r^2$. The Gaussian SCE-I function (or its parabolic variant) is the most commonly used model when fitting visibility measurement data not least because of its elegant

simplicity but also because it makes directly use of the directionality parameter which simplifies the comparison of results with other studies. It has been verified that when an inverse Gaussian SCE-I absorption filter is applied to the eye it is possible to annul the directionality effect observed [94]. Rativa and Vohnsen introduced a modified super-Gaussian function that includes higher-order terms in the exponent to allow flattening of the visibility function and found that it can be adapted to fit experimental results (at short wavelengths where a multi-modal waveguide dependence would be expected) but it also increases the complexity by requiring higher-order directionality parameters [95]. Moon and Spencer introduced a polynomial (conceptually similar to a super-Gaussian) and a non-polynomial function for SCE-I fitting [96] and Enoch introduced a function that improved the quality of fitting for data collected near the pupil rim [52]. The author of this paper has recently introduced a scaled Airy disc distribution as a new fitting function for the SCE-I based on the aperture diffraction model for outer segment layers [28,97] and expressed by

$$\eta(r) = \left(\frac{2J_1(\alpha r)}{\alpha r} \right)^2 \quad \text{Eq. (13)}$$

where to a first approximation $\alpha \approx 2\sqrt{\rho \ln(10)} \approx 3.03\sqrt{\rho}$. The Airy disc function is compared to the Gaussian SCE-I function in Fig. 20.14 and all the various fitting functions are summarized in Table 20.1.

20.7 Visual implications of the Stiles-Crawford effects

In optical models of the eye, the retina is often considered as a screen onto which the anterior eye projects images of the outside world whereby a visual response is triggered. The SCE-I is typically included as a Gaussian pupil apodization notwithstanding that it is of retinal origin. Thus care needs to be taken as the directionality has been determined with Maxwellian illumination which may give rise to differences from that of normal vision. This can be seen

in observed deviations of the integrated Stiles-Crawford effect from the mathematical integration of the SCE-I [52-54]. However, in the healthy eye with small aberrations, and photoreceptors oriented towards a common point, the approach is expected to be valid.

The common explanation of the SCE-I is that it is a mechanism of the eye which serves to dampen the role of intraocular scattering [98] as well as aberrations [99] that could otherwise degrade the effective retinal images captured by the photoreceptor cells. Intensity point-spread function (PSF) analysis and its associated modulation transfer function (MTF) are widespread measures used to determine the role of aberrations and SCE-I pupil apodization when analysing the optics of eye as a function of spatial frequency. For a schematic eye model the PSF (excluding constants) can be expressed as the absolute square of the Fourier Transform (FT) of the pupil function P_{eye} (equal to unity within the circular pupil and zero outside), the wavefront aberrations of the eye Φ_{WA} propagated to the pupil plane, and a Gaussian amplitude pupil apodization $G_{SCE-I}(x,y) = 10^{-\rho\left(x^2+y^2\right)/2}$, i.e.,

$$\begin{aligned} I_{PSF}(u,v) &= \left| \mathrm{FT}_{\frac{n_{eye}u}{\lambda f_{eye}}, \frac{n_{eye}v}{\lambda f_{eye}}} \left\{ P_{eye} G_{SCE-I} \exp\left(i\Phi_{WA}\right) \right\} \right|^2 \\ &= \left| \mathrm{FT}_{\frac{n_{eye}u}{\lambda f_{eye}}, \frac{n_{eye}v}{\lambda f_{eye}}} \left\{ P_{eye} \exp\left(i\Phi_{WA}\right) \right\} * \mathrm{FT}_{\frac{n_{eye}u}{\lambda f_{eye}}, \frac{n_{eye}v}{\lambda f_{eye}}} \left\{ G_{SCE-I} \right\} \right|^2 \end{aligned} \quad \text{Eq. (14)}$$

where $\frac{n_{eye}u}{\lambda f_{eye}}, \frac{n_{eye}v}{\lambda f_{eye}}$ are spatial frequencies for retinal coordinates (u,v) and * denotes a convolution. The convolution produces a smoothening effect of the retinal field amplitude *and* phase when compared to the case of excluding the SCE-I. As the FT of a Gaussian function is itself a Gaussian the pupil apodization corresponds exactly to the smearing of the PSF with a fundamental Gaussian waveguide mode of foveal cones [100] which explains the role of G_{SCE-I} when transferred to the retinal plane. Thus, if higher-order waveguide modes are present, or if there is photoreceptor disarray, the Gaussian pupil apodization would be

invalidated. The MTF can be calculated from the absolute value of the FT of Eq. (14) resulting in (excluding normalization)

$$MTF(u,v) = \left| P_{eye} G_{SCE-I} \exp\left(i\bar{\Phi}_{WA}\right) * P_{eye} G_{SCE-I} \exp\left(-i\Phi_{WA}\right) \right| \qquad \text{Eq. (15)}$$

where the bar above the wavefront aberration in the first term signifies a coordinate inversion ($x \to -x$ and $y \to -y$). From Eq. (15) it can be seen that the SCE-I reduces high-frequency contents in the MTF by damping contributions from light near to the pupil rim [98,101]. Fig. 20.15 shows the impact of the SCE-I on the calculated PSF and MTF without and with the presence of defocus.

Eq. (14) shows that the resulting PSF is sensitive to the wavefront slope at the retina present in $\mathrm{FT}_{\frac{n_{eye}u}{\lambda f_{eye}}, \frac{n_{eye}v}{\lambda f_{eye}}} \left\{ P_{eye} \exp\left(i\Phi_{WA}\right) \right\}$ whether the SCE-I is applied in the pupil plane or is included directly as a photoreceptor convolution in the retinal plane when determining the effective retinal image. Only if replacing $\mathrm{FT}_{\frac{n_{eye}u}{\lambda f_{eye}}, \frac{n_{eye}v}{\lambda f_{eye}}} \left\{ G_{SCE-I} \right\}$ by a delta function (to remove the role of the SCE-I) will the effective PSF be insensitive to any retinal wavefront slope.

For a schematic eye with a circular pupil being uniformly-illuminated by coherent light the field incident on the retina (excluding the pupil SCE-I) can be calculated as

$$\psi_r(u,v) = \frac{4\sqrt{\pi} n_{eye}}{id\lambda f_{eye}} \int_0^{d/2} r \exp(i\Phi_{WA}) J_0\left(\frac{2\pi n_{eye}}{\lambda f_{eye}} r\rho \right) dr \qquad \text{Eq. (16)}$$

where $\rho = \sqrt{u^2 + v^2}$, $r = \sqrt{x^2 + y^2}$ and J_0 is the zeroth-order Bessel function of the first kind. The wavefront aberrations at each pupil point $\left(r\cos\theta, r\sin\theta\right)$ may be expanded as a series of Zernike polynomials Z_q [102] normalized across the pupil radius $d/2$ whereby $\Phi_{WA}(r,\theta) = k\sum_{q=1}^{\infty} c_q Z_q(r,\theta)$ and the c_q's are scaling parameters. When the field with the aberrated wavefront is propagated to the retinal plane only Zernike modes of even radial order (defocus, astigmatism, spherical aberrations,…) will produce a wavefront slope for

light incident on the photoreceptors whereas for odd radial orders (coma, trefoil,…) the wavefront will impinge directly along the axis of each photoreceptor and the image will only be blurred in the field amplitude [100]. Rather than introducing the SCE-I in the pupil plane a Gaussian waveguide mode, ψ_m, will be assumed in each photoreceptor whereby the effective retinal image can be written as $\left|\mathrm{FT}_{\frac{n_{eye}u}{\lambda f_{eye}},\frac{n_{eye}v}{\lambda f_{eye}}}\left\{P_{eye}\exp\left(i\Phi_{WA}\right)\right\}*\psi_{\mathrm{m}}\right|^2$. The incident retinal field from Eq. (16) may be expressed in terms of an amplitude and a phase factor as $\psi_r(u,v)=B(u,v)\exp\left(i\phi_r\left(u,v\right)\right)$. A series expansion of this field at and near the photoreceptor centred at (u_c,v_c) gives that $\psi_r(u,v)\approx B_0(u_c,v_c)\exp\left[i\left(\phi_0+\phi_u\left(u-u_c\right)+\phi_v\left(v-v_c\right)\right)\right]$ where B_0 is the amplitude and ϕ_0 is the phase of the retinal field at the central point of the waveguide entrance facet and the phase derivatives across the waveguide aperture are $\phi_u=\partial\phi/\partial u\big|_{u_c,v_c}$ and $\phi_v=\partial\phi/\partial v\big|_{u_c,v_c}$. In this slowly-varying field approximation the power coupled to the fundamental Gaussian mode of the waveguide can be calculated as

$$P\approx 2\pi\tau w_m^2 B_0^2\exp\left(-\frac{w_m^2}{2}\left(\varphi_u^2+\varphi_v^2\right)\right) \qquad \text{Eq. (17)}$$

where τ is a constant. Examples of using Eq. (17) on the effective PSF are shown in Fig. 20.16 in the presence of different Zernike aberrations.

The exact spatial distribution of visual pigments across the length of outer segments in the cone-rod photoreceptor mosaic makes it challenging to determine exactly where the light will be absorbed when triggering vision. The diameter of photoreceptors is approximately matched to the pupil size and the diffraction limit of resolution. Likewise, a geometrical extension of the conical outer segment of parafoveal cones to the pupil plane is approximately matched to the pupil size [28]. This intricate balance suggests that the entire

outer segment shape may play an important role for vision when the retina is exposed to different lighting conditions [16]. With this in mind the layered light scattering and receiving model can also be used to predict light distributions and estimated visibility across the outer segments [28]. Fig. 20.17 shows the outcome of such an analysis when illuminating a hexagonal packing of layered outer segments with a plane wave being incident on or off axis to simulate the SCE-I and when a focused beam of light is incident on layered outer segments and focused either on or between the photoreceptors to trigger vision. As this approach does not enforce waveguiding, light which is scattered between the receptors may stimulate a visual response even if not directly incident on the photoreceptor in question [103]. It should be noted that self-screening has only been included in the axial absorption in the model as the off-axis angles are small.

The fact that photoreceptors are oriented to capture a maximum of light also means that they are pointing so that wavefront tilt is small or entirely absent at their receiving aperture. This fact has been elegantly shown by Artal *et al*. who found that the eye is best adapted to its own aberrations [102]. Although a neural explanation is argued for, an entirely optical effect based on local photoreceptor pointing adapted to the incident wavefront in the plane of the retina may encompass these findings and agrees qualitatively well with recent observations in retinal tissues [35].

Finally, the role of the SCE-II in a normal visual situation may also be considered by integration of Eqs. (10) – (12) across the pupil when considering a possible hue shift induced by a finite bandwidth of the illumination. However, its influence would be interwoven with the chromatic aberrations of the eye.

20.8 Physical models of the retina

Rather than attempting to study the retina itself under the microscope or using mathematical models for light-tissue interactions, the construction of retinal simulators that would have similar characteristics and be useful to study the role of the Stiles-Crawford effects in a complementary physical setting have been carried out. Such approaches have also inspired biomimetic applications in solar cells [105] and imaging technologies [106]. Physical models of retinal waveguides have been made for use in the microwave range with enlarged waveguides of polystyrene foam to match the cm-range wavelengths employed [107,108] and smaller dielectric rods to match mm-range wavelengths [109] that have all confirmed a directionality similar to that of the SCE-I. Rativa and Vohnsen introduced a liquid-filled photonic crystal fibre as a retinal simulator with waveguide dimensions similar to those of the parafoveal retina and with temperature tuning that allow the exact waveguide parameters to be set from a single to multimode range [110]. This simulator has been used to model the angular dependence of the SCE-I as well as to examine the role of defocus and other aberration modes [111,112]. An example on the use of this simulator is shown in Fig. 20.18.

20.9 Retinal imaging implications of the Stiles-Crawford effects

When light is obliquely incident on the retina photoreceptors reflect less light back through the eye pupil and thus the highest visibility of photoreceptors is obtained when the imaging light enters near the pupil centre [63,113]. Adaptive optics wavefront correction [114,115] and beam apodization [116,117] can be used in scanning retinal imaging applications to match the size of the focused incident beam to the width of the photoreceptors being imaged.

As discussed in Section 20.3, fundus photography, SLO and OCT have all been used to probe photoreceptor directionality [61-64] showing the combined role of an oblique incidence on the individual photoreceptors as well as the directional dependence of the backscattered light. The pigments are commonly bleached or infrared light is used to ensure

that the light traverses the full length of the photoreceptors. It must be stressed that the signal which facilities the visualization of photoreceptors in high resolution retinal images originates in scattering of light from refractive index differences within the photoreceptors themselves which may well have a different directionality than the psychophysical SCE-I. A somewhat open question is the origin of the multi-layered retinal reflections, and in particular the middle band at or near the ellipsoid where high refractive-index mitochondria organelles are located, seen in high-resolution OCT images [5,118,119]. OCT has also revealed reflective gaps in certain outer segments possibly caused by irregular spacing of the membrane invaginations [120] and temporal variations in the photoreceptor brightness believed to originate in changes in the outer-segment length as pigment layers detach from the photoreceptors [121].

The present author has made use of the layered scattering model [28] to also analyse fundus imaging in relation to oblique incidence of light [122]. In doing so it has been assumed that the main contributions to the retinal images are from a maximum of 3 layers spaced at distances that have been chosen to match the reflective layers seen in OCT images. Fig. 20.19 shows examples of calculated fundus images and the same model has been found valid when analysing image brightness in simulated retinal images as a function of the angle of incidence of the light to mimic the SCE-I showing good correspondence with parafoveal measurements of cone photoreceptor directionality.

20.10 Conclusions

Although questions remain on the exact retinal mechanisms involved in the Stiles-Crawford effects as well as their role for vision, imaging and photoreceptor diagnostics, there can be little doubt that they play an active role for our visual system. Although most of this chapter has described their role for the human eye, very similar cellular mechanisms are found in a

wide range of animal eyes ranging from mammals to invertebrates with the latter having directional light-guiding mechanisms in elongated cylindrical rhabdomeres that are located behind the anterior corneal lens where they direct light across visual pigments towards posterior axons [123].

Apart from the photoreceptors in the human retina themselves, another light-guiding mechanism has been identified in the parafoveal Muller glial cells that, due to an increased refractive index, are believed to act as a supportive mechanism to aid the guiding of light across the neural retina towards the photoreceptors with a minimum of perturbations [124] and to contribute with a redistribution of the retinal image to better match the spectral properties of the receiving pigments of the cones and rods [125]. The refractive indices across the Muller cells and their surrounds suggest a multimode waveguide behaviour that is less efficient to confine the light than the photoreceptors. Their directionality is expected to be low and therefore no SCE-I function has yet been assigned to the Muller cells.

In a significant part of this chapter, the possible absence or reduced role of waveguiding in the individual photoreceptors has been analysed based on the fact that the directionality seems to be inherent in the proper organization of the visual pigments themselves and that the role of nonguided components (normally ignored in waveguide models) cannot simply be ignored as it accounts for a significant fraction of the total light transmitted across the retina. Further progress along this line will require improved data on the exact optical properties of the photoreceptors and their surrounds in the living eye and retina as well as more advanced modelling tools. It seems therefore fitting to end this chapter with the insightful statement of Prof. N. Bohr that "…owing to the very limits imposed by the properties of light, no instrument is imaginable which is more efficient for its purpose than the eye" [126] which makes perfect sense considering how the retinal cone and rod photoreceptors have developed

to match the optics of our eye, the light in our environment, and to provide accurate vision in the healthy eye.

Acknowledgments:

I am indebted to my former and current students who have all contributed to my present understanding of the Stiles-Crawford effects. For the work presented here I wish to thank in particular Dr. Diego Rativa, Dr. Benjamin Lochocki, Dr. Sara Castillo, Ms. Denise Valente and Mr. Fabio Rodrigo. I am also very grateful to Prof. Gerald Westheimer and Prof. Jay M. Enoch whose work and insight has inspired me enormously. This research has been made possible thanks to funding from Science Foundation Ireland (grants 07/SK/B1239a and 08/IN.1/B2053).

20.10 References

[1] J K Bowmaker and H J Dartnall, *Visual pigments of rods and cones in human retina*, J. Physiol. **298** (1980) 501– 511.

[2] R. W. Rodieck, "The first steps in seeing" (Sinauer Associates, 1998).

[3] A. M. Laties and J. M. Enoch, *An analysis of retinal receptor orientation. I. Angular relationship of neighboring photoreceptors*, Invest. Ophthalmol. **10** (1971) 69–77.

[4] Q. V. Hoang, R. A. Linsenmeier, C. K. Chung CK, and C. A. Curcio, *Photoreceptor inner segments in monkey and human retina: mitochondrial density, optics, and regional variation*, Vis Neurosci. **19** (2002) 395-407.

[5] D. C. Hood, X. Zhang, R. Ramachandran, C. L. Talamini, A. Raza, J. P. Greenberg, J. Sherman, S. H. Tsang, and D. G. Birch, *The inner segment/outer segment border seen on optical coherence tomography is less intense in patients with diminished cone function*, Invest. Ophthalmol. Vis. Sci. **52** (2011) 9703–9709.

[6] J. J. Wolken, "Light detectors, photoreceptors and imaging systems in nature" (Oxford University, 1995).

[7] D. Fotiadis, Y. Liang, S. Filipek, D. A. Saperstein, A. Engel, and K. Palczewski, *Atomic-force microscopy: Rhodopsin dimers in native disc membranes*, Nature **421** (2003) 127–128.

[8] R. W. Young, *The renewal of rod and cone outer segments in the rhesus monkey*, J. Cell Biol. **49** (1971) 303-318.

[9] J. Nguyen-Legros and D. Hicks, *Renewal of photoreceptor outer segments and their phagocytosis by the retinal pigment epithelium*, Int. Rev. Cytology **196** (2000) 245-313.

[10] C. A. Curcio, K. R. Sloan, R. E. Kalina, A. E. Hendrickson, *Human photoreceptor topography*, J. Comp. Neurol. **292** (1990) 497–523.

[11] W. S. Stiles, B. H. Crawford, *The luminous efficiency of rays entering the eye pupil at different points*, Proc. R. Soc. London B **112** (1933) 428–450.

[12] W. D. Wright and J. H. Nelson, *The relation between the apparent intensity of a beam of light and the angle at which the beam strikes the retina*, Proc. Phys. Soc. **48** (1936) 401-424.

[13] R. A. Applegate, V. Lakshminarayanan, *Parametric representation of Stiles–Crawford functions: normal variation of peak location and directionality*, J. Opt. Soc. Am. A **10**, (1993) 1611–1623.

[14] W. S. Stiles, *The luminous efficiency of monochromatic rays entering the eye pupil at different points and a new colour effect*, Proc. R. Soc. London B **123** (1937) 90–118.

[15] B. H. Crawford, *The luminous efficiency of light rays entering the eye pupil at different points and its relation to brightness threshold measurements*, Proc. Roy. Soc. B **124** (1937) 81-96.

[16] G. Westheimer, *Dependence of the magnitude of the Stiles-Crawford effect on retinal location*, J. Physiol. **192** (1967) 309-315.

[17] J. M. Enoch and G. M. Hope, *Directional sensitivity of the foveal and parafoveal retina*, Invest. Ophthalmol. Vis. Sci. **12** (1973) 497-503.

[18] F. Flamant and W. S. Stiles, *The directional and spectral sensitivities of the retinal rods to adapting fields of different wave-lengths*, J. Physiol. **107** (1948) 187-202.

[19] J. A. Van Loo, Jr. and J. M. Enoch, *The scotopic Stiles-Crawford effect*, Vision Res. **15** (1975) 1005-1009.

[20] G. Hansen, *Zur Kenntnis des physiologischen Apertur-Farbeffektes Stiles-Crawford-Effekt II. Art*, Naturwissenschaften **31** (1943) 416-417.

[21] G. Toraldo di Francia and L. Ronchi, *Directional scattering of light by the human retina*, J. Opt. Soc. Am. **42** (1952) 782–783.

[22] S. A. Burns, S. Wu, F. Delori, A. E. Elsner, *Direct measurement of human-cone-photoreceptor alignment*, J. Opt. Soc. Am. A **12** (1995) 2329–2338.

[23] S. Marcos, S. A. Burns, *Cone spacing and waveguide properties from cone directionality measurements*, J. Opt. Soc. Am. A **16** (1999) 995–1004.

[24] N. P. A. Zagers, J. van de Kraats, T. T. J. M. Berendschot, D. van Norren, *Simultaneous measurement of foveal spectral reflectance and cone-photoreceptor directionality*, Appl. Opt. **41** (2002) 4686–4696.

[25] J.-M. Gorrand and M. Doly, *Alignment parameters of foveal cones*, J. Opt. Soc. Am. A **26** (2009) 1260-1267.

[26] B. Vohnsen, I. Iglesias, and P. Artal, *Guided light and diffraction model of human-eye photoreceptors*, J. Opt. Soc. Am. A **22** (2005) 2318-2328.

[27] B. Vohnsen, *On the spectral relation between the first and second Stiles–Crawford effect*, J. Mod. Opt. **56** (2009) 2261-2271.

[28] B. Vohnsen, *Directional sensitivity of the retina: A layered scattering model of outer-segment photoreceptor pigments*, Biomed. Opt. Express **5** (2014) 1569-1587.

[29] J. Mod. Opt. **56** (2009) pp. 2159-2308. Special Issue: The Stiles–Crawford Effects and Photoreceptor Optics: A celebration of the 75th anniversary of the discovery of the Stiles–Crawford Effect.

[30] G. Westheimer, *Directional sensitivity of the retina: 75 years of Stiles-Crawford effect*, Proc. R. Soc. B **275** (2008) 2777–2786.

[31] E. W. Brücke, *Ueber die physiologische Bedeutung der stabförmigen Körper und der Zwillingszapfen in den Augen der Wirbelthiere*, Archiv für Anatomie, Physiologie und wissenschaftliche Medicin (1844) 444-451.

[32] H. von Helmholtz, "Treatise on Physiological Optics" (Dover Publications, 1962).

[33] H. S. Smallman, D. I. A. MacLeod and P. Doyle, *Vision: Realignment of cones after cataract removal*, Nature **412** (2001) 604-605.

[34] M. Kono, J. M. Enoch, E. Strada, P. Shih, R. Srinivasan, V. Lakshminarayanan, W. Susilasate and A. Graham, *Stiles-Crawford effect of the first kind: assessment of photoreceptor alignments following dark patching*, Vision Res. **41** (2001) 103-118.

[35] B. Wang, Q. Zhang, R. Lu, Y. Zhi, and X. Yao, *Functional optical coherence tomography reveals transient phototropic change of photoreceptor outer segments*, Opt. Lett. **39** (2014) 6923-6926.

[36] A. Hannover, *Mikroskopiske undersøgelser af nervesystemet*, Kong. Danske Videns. Sels. Naturv. Math. Afh. **X** (1843) 1-111.

[37] J. M. Enoch, *Wave-guide modes in retinal receptors*, Science **133** (1961) 1353-1354.

[38] J. M. Enoch, *Optical properties of the retinal receptors*, J. Opt. Soc. Am. **53** (1963) 71–85.

[39] O. S. Packer, D. R. Williams, and D. G. Bensinger, *Photopigment transmittance imaging of the primate photoreceptor mosaic*, J. Neurosci.**16** (1996) 2251–2260.

[40] G. Westheimer, *The maxwellian view*, Vision Res. **6** (1966) 669-682.

[41] B. Lochocki, D. Rativa, and B. Vohnsen, *Spatial and spectral characterisation of the first and second Stiles-Crawford effects using tuneable liquid-crystal filters*, J. Mod. Opt. **58** (2011) 1817-1825.

[42] B. Lochocki and B. Vohnsen, *Defocus-corrected analysis of the foveal Stiles–Crawford effect of the first kind across the visible spectrum*, J. Opt. **15** (2013) 125301.

[43] N. Singh, D. A. Atchison, S. Kasthurirangan and H. Guo, *Influences of accommodation and myopia on the foveal Stiles–Crawford effect*, J. Mod. Opt. **56** (2009) 2217–2230.

[44] B. Lochocki and B. Vohnsen, "The 1st Stiles-Crawford effect: A single beam frequency flickering system" in Proc. VII European / I World Meeting in Visual and Physiological

Optics, R. Iskander and H. T. Kasprzak, Eds., ISBN: 978-83-7493-847-1 (2014) pp. 183-185.

[45] D. G. Birch, M. A. Sandberg, and E. L. Berson, *The Stiles-Crawford effect in retinitis pigmentosa*, Invest. Ophthalmol. Vis. Sci. **22** (1982) 157-164.

[46] D. L. McCulloch and V. Lakshminarayanan, *The Stiles-Crawford effect of the first kind and the full-field electroretinogram (ERG)*, J. Mod. Opt. **56** (2009) 2176-2180.

[47] C. S. Matsumoto, K. Shinoda, H. Matsumoto, S. Satofuka, A. Mizota, K. Nakatsuka, and Y. Miyake, *Stiles–Crawford effect in focal macular ERGs from macaque monkey*, J. Vision **12** (2012) 6.

[48] W. L. Makous, *A transient Stiles-Crawford effect*, Vision Res. **8** (1968) 1271–1284.

[49] P. L. Walraven, *Recovery from the increase of the Stiles-Crawford effect after bleaching*, Nature **210** (1966) 311–312.

[50] P. J. de Groot, *Transient threshold increase due to combined changes in direction of propagation and plane of polarization*, Vision Res. **19** (1979) 1253-1259.

[51] J. Gordon and I. Abramov, *Color appearance: Maxwellian vs. Newtonian views*, Vision Res. **48** (2008) 1879-1883.

[52] J. M. Enoch, *Summated response of the retina to light entering different parts of the pupil*, J. Opt. Soc. Am. **48** (1958) 392–405.

[53] B. Drum, *Additivity of the Stiles–Crawford effect for a Fraunhofer image*, Vision Res. **15** (1975) 291–298.

[54] B. Vohnsen, B. Lochocki, and C. Vela, "Integrated Stiles-Crawford effect in normal vision" in Proc. VII European / I World Meeting in Visual and Physiological Optics, R. Iskander and H. T. Kasprzak, Eds., ISBN: 978-83-7493-847-1 (2014) pp. 368-371.

[55] B. Vohnsen and D. Rativa, *Absence of an integrated Stiles-Crawford function for coherent light*, J. Vis. **11** (2011) 19.

[56] S. Castillo and B. Vohnsen, *Exploring the Stiles-Crawford effect of the first kind with coherent light and dual Maxwellian sources*, Appl. Opt. **52** (2013) A1–A8.

[57] G. Westheimer, *Retinal light distributions, the Stiles–Crawford effect and apodization*, J. Opt. Soc. Am. A **30** (2013) 1417-1421.

[58] J. M. Enoch and W. S. Stiles, *The colour change of monochromatic light with retinal angle of incidence*, Opt. Acta **8** (1961) 329–358.

[59] G. J. van Blockland and D. van Norren, *Intensity and polarization of light scattered at small angles from the human fovea*, Vision Res. **26** (1986) 485-494.

[60] J.-M. Gorrand and F. Delori, *A reflectometric technique for assessing photoreceptor alignment*, Vision Res. **35** (1995) 999–1010.

[61] P. J. Delint, T. T. J. M. Berendschot, and D. van Norren, *Local photoreceptor alignment measured with a scanning laser ophthalmoscope*, Vision Res. **37** (1997) 243-248.

[62] W. Gao, B. Cense, Y. Zhang, R. S. Jonnal, and D. T. Miller, *Measuring retinal contributions to the optical Stiles-Crawford effect with optical coherence tomography*, Opt. Express **16** (2008) 6486-6501.

[63] A. Roorda and D. R. Williams, *Optical fiber properties of individual human cones*, J. Vision **2** (2002) 404-412.

[64] D. Rativa and B. Vohnsen, *Analysis of individual cone-photoreceptor directionality using scanning laser ophthalmoscopy*, Biomed. Opt. Express **2** (2011) 1423-1431.

[65] F. Schaeffel, A. Glasser, and H. C. Howland, *Accommodation, refractive error and eye growth in chickens*, Vision Res. **28** (1988) 639-657.

[66] E. F. Fincham, *The accommodation reflex and its stimulus*, Br. J. Ophthalmol. **35** (1951) 381-393.

[67] P. B. Kruger, N. Lopez-Gil and L. R. Stark, *Accommodation and the Stiles-Crawford effect: theory and a case study*, Ophthal. Physiol. Opt. **21** (2001) 339-351.

[68] K. Blank, R. R. Provine, and J. M. Enoch, *Shift in the peak of the photopic Stiles-Crawford function with marked accommodation*, Vision Res. **15** (1975) 499-507.

[69] S. S. Choi, L. F. Garner, and J. M. Enoch, *The relationship between the Stiles-Crawford effect of the first kind (SCE-I) and myopia*, Ophthal. Physiol. Opt. **23** (2003) 465-472.

[70] V. C. Smith, J. Pokorny, and K. R. Diddie, *Color matching and the Stiles–Crawford effect in observers with early age-related macular changes*, J. Opt. Soc. Am. A **5** (1988) 2113-2121.

[71] P. K. DeLint, T. T. Berendschot, and D. van Norren, *A comparison of the optical Stiles-Crawford effect and retinal densitometry in a clinical setting*, Invest. Ophthalmol. Vis. Sci. **39** (1998) 1519-1523.

[72] B. O'Brien, *A theory of the Stiles and Crawford effect*, J. Opt. Soc. Am. **36** (1946) 506-509.

[73] A. Safir and L. Hyams, *Distribution of cone orientations as an explanation of the Stiles–Crawford effect*, J. Opt. Soc. Am. **59** (1969) 757–765.

[74] G. Toraldo di Francia, *Retina cones as dielectric antennas*, J. Opt. Soc. Am. **39** (1949) 324.

[75] R. Röhler and W. Fischer, *Influence of waveguide modes on the light absorption in photoreceptors*, Vision Res. **11** (1971) 97-101.

[76] A. W. Snyder and C. Pask, *The Stiles-Crawford effect: Explanation and consequences*, Vision Res. **13** (1973) 1115-1137.

[77] A. W. Snyder and C. Pask, *Waveguide modes and light absorption in photoreceptors*, Vision Res. **13** (1973) 2605-2608.

[78] W. Wijngaard, *Some normal modes of an infinite hexagonal array of identical circular dielectric rods*, J. Opt. Soc. Am. **64** (1974) 1136-1144.

[79] L. Fischer, A. Zvyagin, T. Plakhotnik, and M. Vorobyev, *Numerical modeling of light propagation in a hexagonal array of dielectric cylinders*, J. Opt. Soc. Am. A **27** (2010) 865-872.

[80] R. L. Sidman, *The structure and concentration of solids in photoreceptor cells studied by refractometry and interference microscopy*, J. Biophys. Biochem. Cytol. **3** (1957) 15-30.

[81] C. Pask and A. W. Snyder, "Theory of the Stiles–Crawford effect of the second kind," in Photoreceptor Optics, A. W. Snyder and R. Menzel, eds. (Springer-Verlag, 1975), pp. 152–156.

[82] R. Sammut and A. W. Snyder, *Contribution of unbound modes to light absorption in visual photoreceptors*, J. Opt. Soc. Am. **64** (1974) 1711-1714.

[83] W. Fischer and R. Röhler, *The absorption of light in an idealized photoreceptor on the basis of waveguide theory – II: The semi-infinite cylinder*, Vision Res. **14** (1974) 1115-1125.

[84] M. P. Rowe, N. Engheta, S. S. Easter, Jr., and E. N. Pugh, Jr., *Graded-index model of a fish double cone exhibits differential polarization sensitivity*, J. Opt. Soc. Am. A **11** (1994) 55–70.

[85] J. J. Vos and F. L. van Os, *The effect of lens density on the Stiles-Crawford effect*, Vision Res. **15** (1975) 749-751.

[86] A. M. Pozo, F. Pérez-Ocón, and J. R. Jiménez, *FDTD analysis of the light propagation in the cones of the human retina: an approach to the Stiles-Crawford effect of the first kind*, J. Opt. A: Pure Appl. Opt. **7** (2005) 357-363.

[87] M. J. Piket-May, A. Taflove, and J. B. Troy, *Electrodynamics of visible-light interactions with the vertebrate retinal rod*, Opt. Lett. **18** (1993) 568–570.

[88] J. M. Enoch, *Waveguide modes: are they present, and what is their possible role in the visual mechanism?*, J. Opt. Soc. Am. **50** (1960) 1025-1026.

[89] T. T. J. M. Berendschot, J. van de Kraats, and D. Van Norren, *Wavelength dependence of the Stiles–Crawford effect explained by perception of backscattered light from the choroid*, J. Opt. Soc. Am. A **18** (2001) 1445–1451.

[90] B. Chen and W. Makous, *Light capture by human cones*, J. Physiol. **414** (1989) 89-109.

[91] J. R. Coble and W. A. H. Rushton, *Stiles-Crawford effect and the bleaching of cone pigments*, J. Physiol. **217** (1971) 231-242.

[92] P. L. Walraven and M. A. Bouman, *Relation between Directional Sensitivity and Spectral Response Curves in Human Cone Vision*, J. Opt. Soc. Am. **50** (1960) 780-784.

[93] M. Alpern, *The Stiles-Crawford effect of the second kind (SCII): a review*, Perception **15** (1986) 785-799.

[94] D. A. Atchison, D. H. Scott, N. C. Strang, and P. Artal, *Influence of Stiles–Crawford apodization on visual acuity*, J. Opt. Soc. Am. A **19** (2002) 1073–1083.

[95] D. Rativa and B. Vohnsen, *Single- and multimode characteristics of the foveal cones: the super-Gaussian function*, J. Mod. Opt. **58** (2011) 1809-1816.

[96] P. Moon and D. E. Spencer, *On the Stiles-Crawford effect*, J. Opt. Soc. Am. **34** (1944) 319-329.

[97] B. Vohnsen, "Multi-aperture model of photoreceptor outer segments" in Proc. VII European / I World Meeting in Visual and Physiological Optics, R. Iskander and H. T. Kasprzak, Eds., ISBN: 978-83-7493-847-1 (2014) pp. 372-375.

[98] H. Metcalf, *Stiles-Crawford apodization*, J. Opt. Soc. Am. **55** (1965) 72-74.

[99] X. Zhang, M. Ye, A. Bradley, and L. Thibos, *Apodization by the Stiles–Crawford effect moderates the visual impact of retinal image defocus*, J. Opt. Soc. Am. A **16** (1999) 812–820.

[100] B. Vohnsen, *Photoreceptor waveguides and effective retinal image quality*, J. Opt. Soc. Am. A **24** (2007) 597–607.

[101] J. P. Carroll, *Apodization model of the Stiles-Crawford effect*, J. Opt. Soc. Am. **70** (1980) 1155-1156.

[102] R. J. Noll, *Zernike polynomials and atmospheric turbulence*, J. Opt. Soc. Am. **66** (1976) 207-211.

[103] W. M. Harmening, W. S. Tuten, A. Roorda, and L. C. Sincich, *Mapping the perceptual grain of the human retina*, J. Neurosci. **34** (2014) 5667-5677.

[104] P. Artal, L. Chen, E. J. Fernández, B. Singer, S. Manzanera, and D. R. Williams, *Neural compensation for the eye's optical aberrations*, J. Vision **4** (2004) 281-287.

[105] V. G. Kravets and A. N. Grigorenko, *Retinal light trapping in textured photovoltaic cells*, Appl. Phys. Lett. **97** (2010) 133701.

[106] P. Kornreich and B. Farell, *True three-dimensional camera*, J. Electron. Imaging **22** (2013) 013028.

[107] B. O'Brien, *Vision and resolution in the central retina*, J. Opt. Soc. Am. **41** (1951) 882–894.

[108] J. M. Enoch and G. A. Fry, *Characteristics of a model retinal receptor studied at microwave frequencies*, J. Opt. Soc. Am. **48** (1958) 899–911.

[109] P. J. de Groot and R. E. Terpstra, *Millimeter-wave model of a foveal receptor*, J. Opt. Soc. Am. **70** (1980) 1436-1452.

[110] D. Rativa and B. Vohnsen, *Simulating human photoreceptor optics using a liquid-filled photonic crystal fiber*, Biomed. Opt. Express **2** (2011) 543–551.

[111] B. Vohnsen, D. Rativa, C. Vela, B. Lochocki, and P. Kruger, *The role of defocus on photoreceptor light coupling analyzed with a waveguide-based retinal simulator*, ARVO-abstract **3429-C0150** (2013).

[112] D. Valente, D. Rativa, and B. Vohnsen, "The role of defocus analyzed with a waveguide-based retinal simulator" in Proc. VII European / I World Meeting in Visual and Physiological Optics, R. Iskander and H. T. Kasprzak, Eds., ISBN: 978-83-7493-847-1 (2014) pp. 357-360.

[113] B. Vohnsen, I. Iglesias, and P. Artal, *Directional imaging of the retinal cone mosaic*, Opt. Lett. **29** (2004) 968-970.

[114] A. Roorda, F. Romero-Borja, W. J. Donnelly III, H. Queener, T. J. Hebert, and M. C. W. Campbell, *Adaptive optics scanning laser ophthalmoscopy*, Opt. Express **10** (2002) 405-412.

[115] A. Dubra, Y. Sulai, J. L. Norris, R. F. Cooper, A. M. Dubis, D. R. Williams, and J. Carroll, *Noninvasive imaging of the human rod photoreceptor mosaic using a confocal adaptive optics scanning ophthalmoscope*, Biomed. Opt. Express **2** (2011) 1864–1876.

[116] B. Vohnsen and D. Rativa, *Ultrasmall spot size scanning laser ophthalmoscopy*, Biomed. Opt. Express **2** (2011) 1597-1609.

[117] Y. N. Sulai and A. Dubra, *Adaptive optics scanning ophthalmoscopy with annular pupils*, Biomed. Opt. Express 3 (2012) 1647-1661.

[118] R. F. Spaide and C. A. Curcio, *Anatomical correlates to the bands seen in the outer retina by optical coherence tomography: literature review and model*, Retina **31** (2011) 1609-1619.

[119] R. S. Jonnal, O. P. Kocaoglu, R. J. Zawadzki, S.-H. Lee, J. S. Werner, and D. T. Miller, *The cellular origins of the outer retinal bands in optical coherence tomography images*, Invest. Ophthalmol. Vis. Sci. **14** (2014) 14907.

[120] M. Pircher, E. Götzinger, H. Sattmann, R. A. Leitgeb, and C. K. Hitzenberger, *In vivo investigation of human cone photoreceptors with SLO/OCT in combination with 3D motion correction on a cellular level*, Biomed. Opt. Express **18** (2010) 13935–13944.

[121] R. S. Jonnal, J. R. Besecker, J. C. Derby, O. P. Kocaoglu, B. Cense, W. Gao, Q. Wang, and D. T. Miller, *Imaging outer segment renewal in living human cone photoreceptors*, Opt. Express **18** (2010) 5227-5270.

[122] B. Vohnsen, *Modeling photoreceptor mosaic imaging as backscattering of light from multilayered discs*, Frontiers in Optics abstract (2014) abstract FW5F.5.

[123] D. G. Stavenga, *Waveguide modes and refractive index in photoreceptors of invertebrates*, Vision Res. **15** (1975) 323-330.

[124] K. Franze, J. Grosche, S. N. Skatchkov, S. Schinkinger, C. Foja, D. Schild, O. Uckerman, K. Travi, A. Reichenbac and J. Guck, *Müller cells are living optical fibers in the vertebrate retina*, Proc. Nat. Ac. Sci. **104** (2007) 8287-8292.

[125] A. M. Labin, S. K. Safuri, E. N. Ribak, and I. Perlman, *Müller cells separate between wavelengths to improve day vision with minimal effect upon night vision*, Nature Communications **5** (2014) 4319.

[126] N. Bohr, *Light and life*, Nature **131** (1933) 457–459.

Figures:

Fig. 20.1: Normalized spectral sensitivities of the S, M and L cone pigments based on data from Ref. [1] (left) and the associated CIE V-λ luminosity function with highest sensitivity at 555 nm wavelength (right).

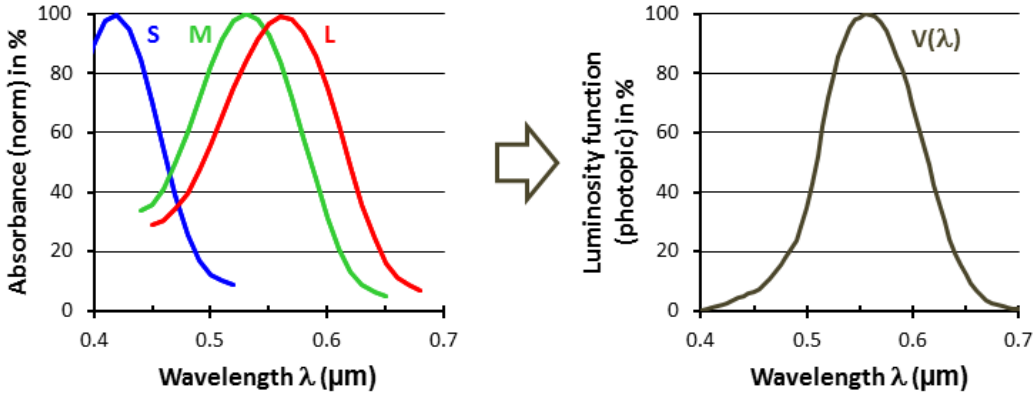

Fig. 20.2: Histological images of the parafoveal rod-cone photoreceptor mosaic: side view (left) and front view (middle) by courtesy of Dr. Peter Munro, Institute of Ophthalmology, University College London, UK. Also shown (right) is a zoom-in on dense outer-segment pigment layers above which large mitochondria cells can be seen. This figure has been reproduced with permission from Fig. 3 in Roy H. Steinberg, Steven K. Fisher, and Don H. Anderson, *Disc morphogenesis in vertebrate photoreceptors*, J. Comp. Neurol. **190** ©1980 John Wiley and Sons.

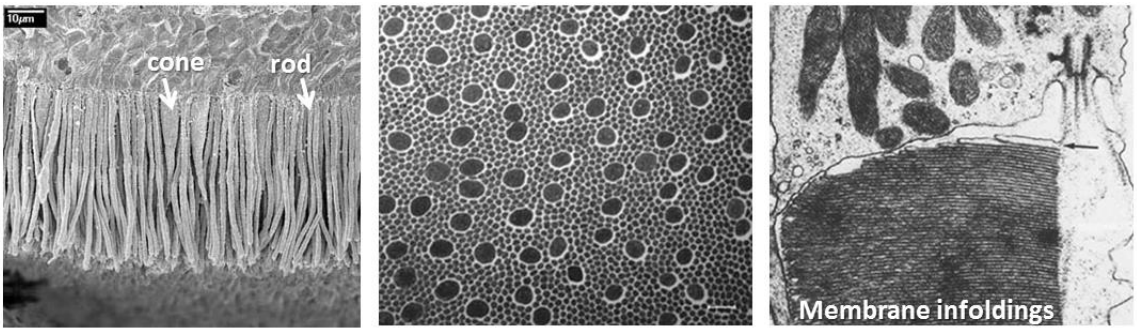

Fig. 20.3: Photopic and scotopic SCE-I visibility data (semi-log plot) for one subject at 6° nasal obtained with orange-red light. For photopic conditions the directionality is $\rho \approx 0.045\,/\,\mathrm{mm}^2$ whereas for scotopic conditions it is $\rho \approx 0.010\,/\,\mathrm{mm}^2$ (but only half of that if the outer-most points are excluded, in which case the distribution is almost flat). Redrawn with permission from Fig. 5 in Joseph A. Van Loo and Jay M. Enoch, *The scotopic Stiles-Crawford effect*, Vision Res. **15** ©1975 Elsevier.

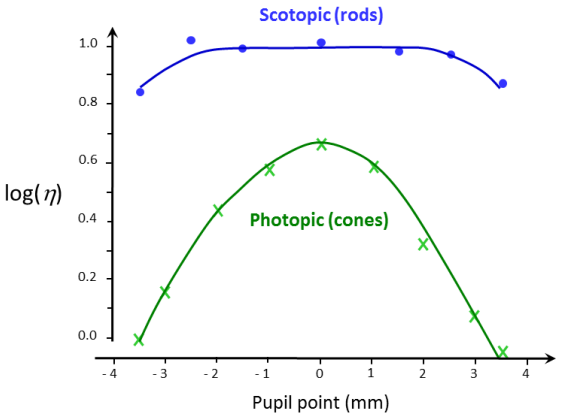

Fig. 20.4: Waveguide intensity distributions measured in transmission (bottom) from outer segments in retinal tissues (rat, monkey and human) compared with the theoretical expectations based on individual cylindrical waveguide modes (top). The associated *V*-number increases from left (single mode) to right (multimode). Reproduced with permission from Fig. 6 in Jay M. Enoch, *Optical properties of the retinal photoreceptors*, Journal of the Optical Society of America **53** ©1963 Optical Society of America.

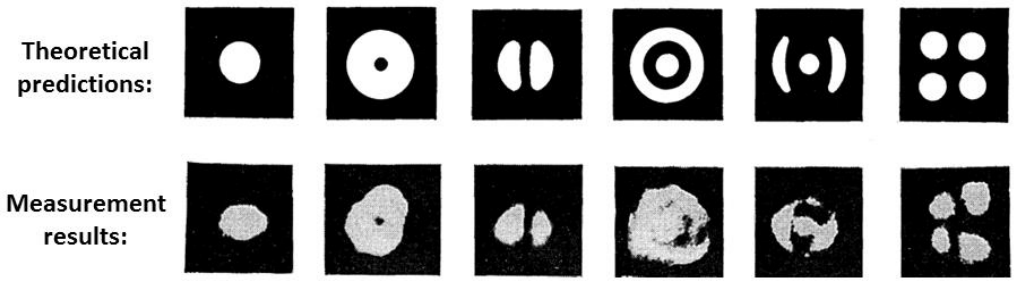

Fig. 20.5: Schematic comparison between bipartite (left) and flicker (right) methods for SCE-I characterization and their visual appearance to the subject. In the bipartite configuration the test and reference half-fields are compared in brightness and the test (or reference) is adjusted until the two appear as equally bright. In the flicker methodology the reference and test fields appear sequentially so at any instant in time only the test or the reference is seen. Their brightness (or time of appearance) is matched until the flicker becomes unnoticeable.

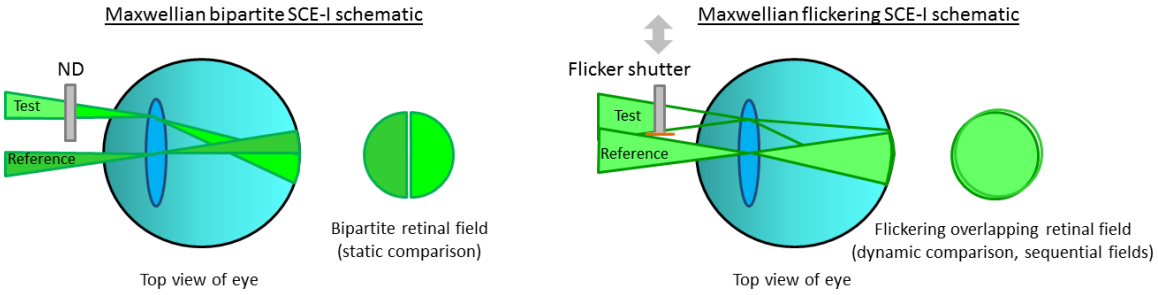

Fig. 20.6: Calculated intensities (left) at the pupil for a 5 mm annular (a,b,c), semi-annular (d,e,f) and point-like (g,h,i) Maxwellian illumination with randomized phase and corresponding retinal images (33µm × 33µm) showing the intensity and phase (2π-wrapped) in the retinal field. Yellow circles mark selected bright speckles and their corresponding phase maps of the wavefront across them. Corresponding SCE-I measurement results (right) for the author's right eye showing a partial (semi-annular) and complete (annular) SCE-I cancellation once the wavefront tilt across the speckles is absent. The directionality parameter decreases from 0.051/mm^2 (Maxwellian point) to 0.019/mm^2 (semi-annular) and to 0.0008/mm^2 (annular). The simulations and the experiments used a 632.8nm wavelength (HeNe laser) except for the Maxwellian point results that have been obtained in a bipartite setup using a tungsten-halogen source and a 620nm wavelength filter (10nm bandpass). Reproduced from Figs. 3 and 7 in B. Vohnsen and D. Rativa, *Absence of an integrated Stiles-Crawford function for coherent light*, J. Vision **11** article 19 with permission from the Association for Research in Vision and Ophthalmology ©2011 ARVO.

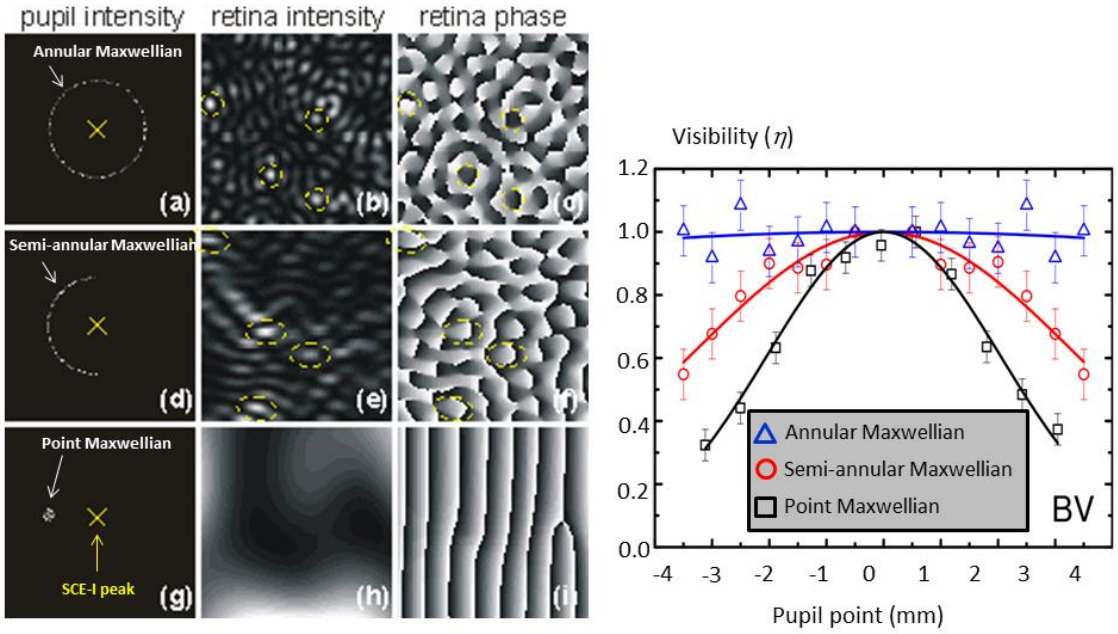

Fig. 20.7: SCE-I and SCE-II measurement results for the author's right eye at three selected wavelengths. The directionality parameter is in the range of 0.029 – 0.045/mm^2 dependent on the wavelength and bandwidth (with defocus corrected the directionality increases to about 0.050 – 0.068/mm^2 [42]). In the SCE-II plots, results from Stiles (1937) have been included for comparison (at 457, 542 and 636 nm wavelengths: yellow curves) with the hue shift expressed in nm-units. The bandwidth of the colour filters used increases with wavelength. Solid lines (solid square symbols) have been obtained with a wide-bandwidth setting whereas dashed lines (open square symbols) have been obtained with a narrow-bandwidth setting of the illumination. The SCE-I images have been reproduced with permission from Fig. 4 in Lochocki, Rativa and Vohnsen, *Spatial and spectral characterisation of the first and second Stiles–Crawford effects using tuneable liquid-crystal filters*, J. Mod. Opt. **58** ©2011 Taylor & Francis.

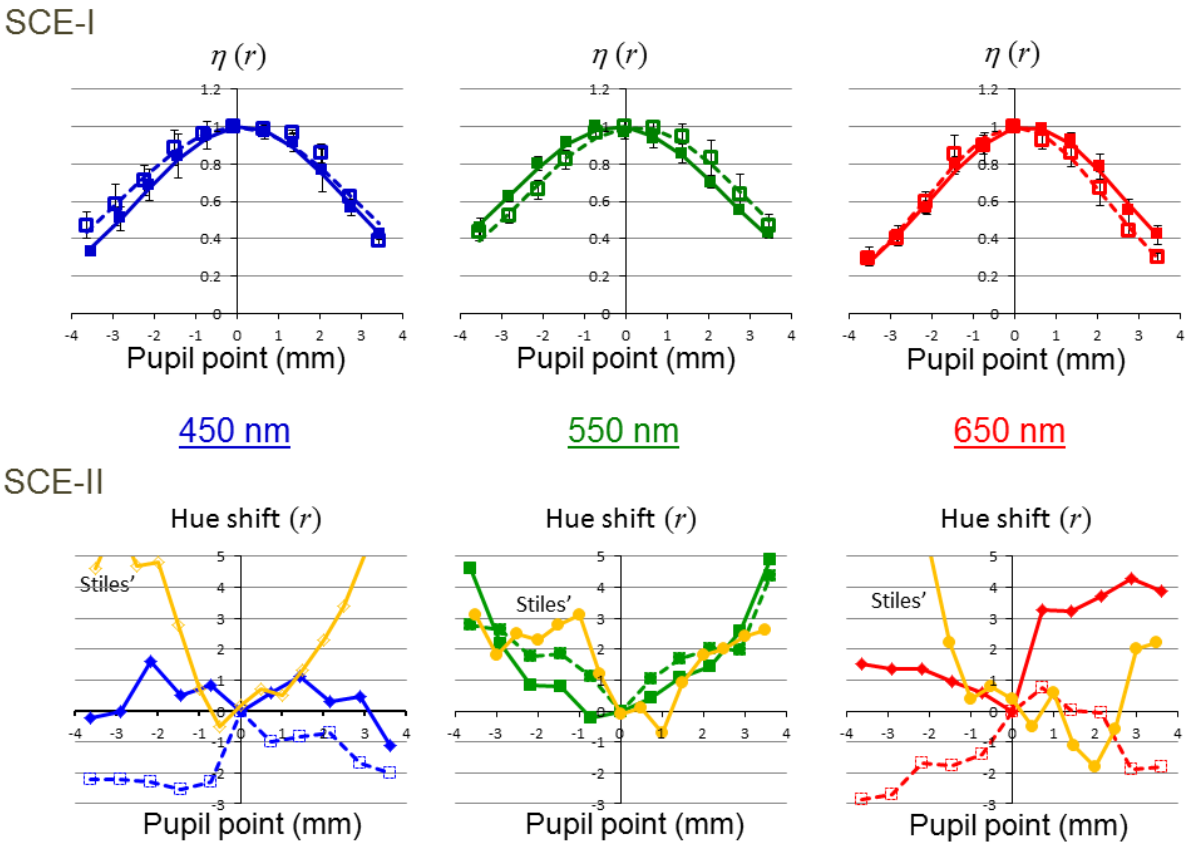

Fig. 20.8: Schematic of expected cone pointing in eyes having short or large axial length (assuming that cones are packed equally dense).

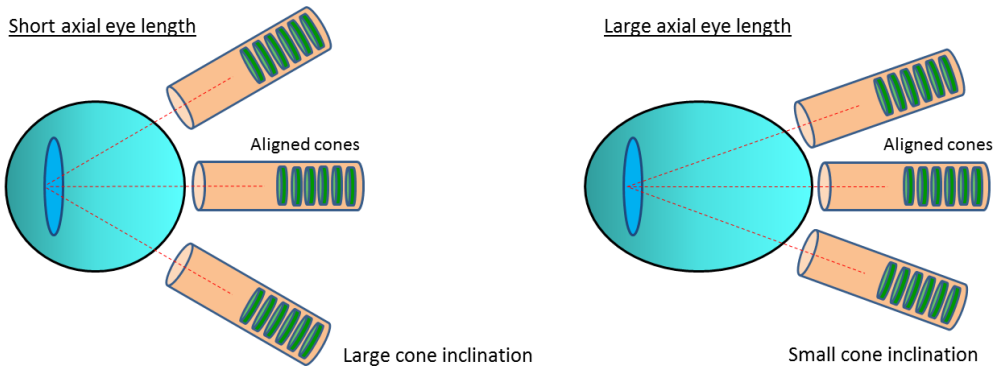

Fig. 20.9: Angular dependence of light coupling to different linear-polarized modes in a cylindrical waveguide and corresponding modal waveguide intensities. The chosen waveguide has $V = 7$ (representative of the inner segment of parafoveal cones). For on-axis incidence, light couples only to the fundamental mode LP_{01} and, when present, LP_{02}. The Gaussian angular dependence expressed by the SCE-I function is approximated by the coupling efficiency for the fundamental mode (foveal cones with a small V) or by its sum for all modes (for large V).

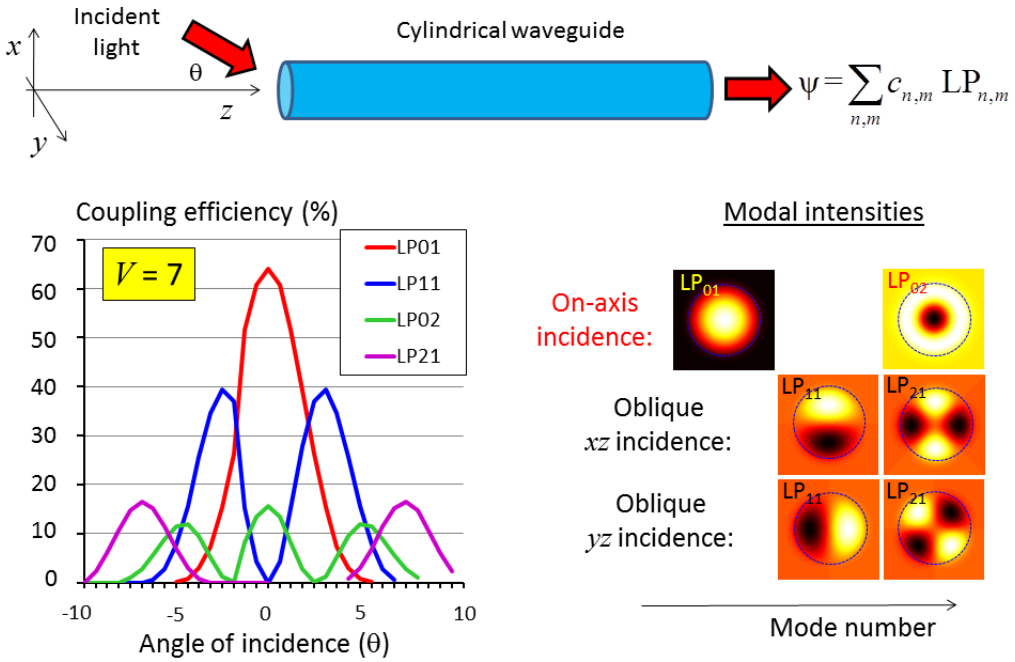

Fig. 20.10: Three different cases of light coupling for an incident Gaussian beam to the Gaussian mode of a cylindrical waveguide. The transmitted power fraction is expressed by the function T. The directionality is $\rho = 2\log(e)\left(\frac{\pi n_{eye}}{\lambda f_{eye}}\right)^2\left(\frac{w_r^2 w_m^2}{w_r^2 + w_m^2}\right)$.

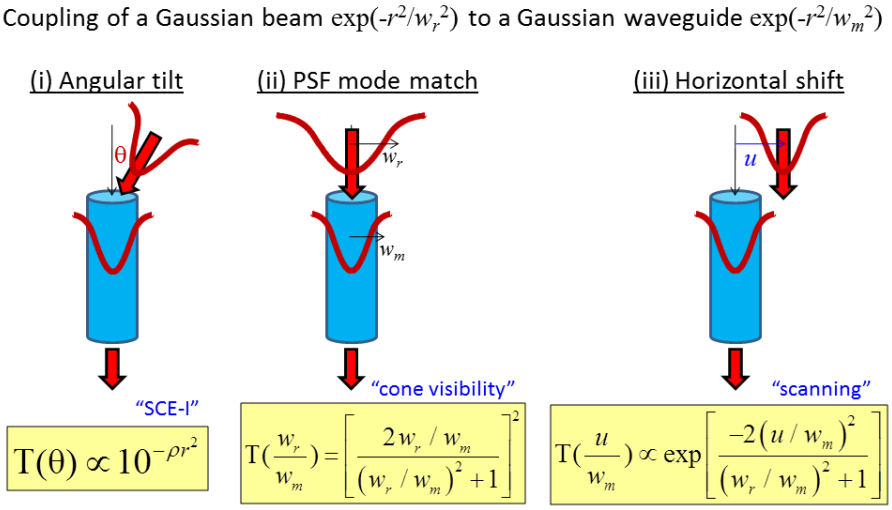

Fig. 20.11: Spectral dependence of the directionality parameter from measurements by Stiles (left) and from waveguide predictions (right) showing a similar though more pronounced reduction in directionality in the green-orange wavelength range. The dependence found by Stiles (Fig. 7 in [14]) has been reproduced with permission by the Royal Society, UK. The single cone and cone distribution plots (the latter with contributions from 5 different waveguide diameters) have been reproduced with permission from Fig. 2 in Brian Vohnsen, *On the spectral relation between the first and second Stiles–Crawford effect*, J. Mod. Opt. **56** ©2009 Taylor & Francis.

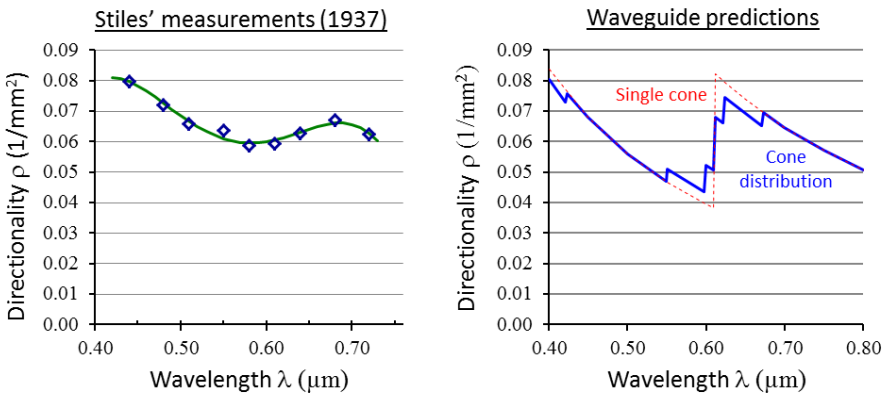

Fig. 20.12: Layered scattering model showing calculated pupil intensity distributions at $\lambda = 550\text{nm}$ for a foveal outer segment in a schematic eye model. The chosen outer segment has dimensions $L = 40\mu\text{m}$, $d_w = 2\mu\text{m}$, and $N = 2000$. Beer-Lambert's law has been employed to show the role of bleaching (left) to modify the contribution from deeply located layers. This shows that for dim light the SCE-I directionality is low ($\rho = 0.066/\text{mm}^2$: blue curve) whereas when fully bleached the directionality is high ($\rho = 0.113/\text{mm}^2$: red curve) as representative of the OSCE. The directionality is lower for a shorter outer segment if its diameter is kept unaltered (e.g., for $L = 20\mu\text{m}$ the directionality becomes $\rho = 0.0585/\text{mm}^2$ and $\rho = 0.0759/\text{mm}^2$, respectively, for the same two cases of low or high bleach). The number of outer-segment layers included in the calculation (right) plays no significant role once $N \geq 10$.

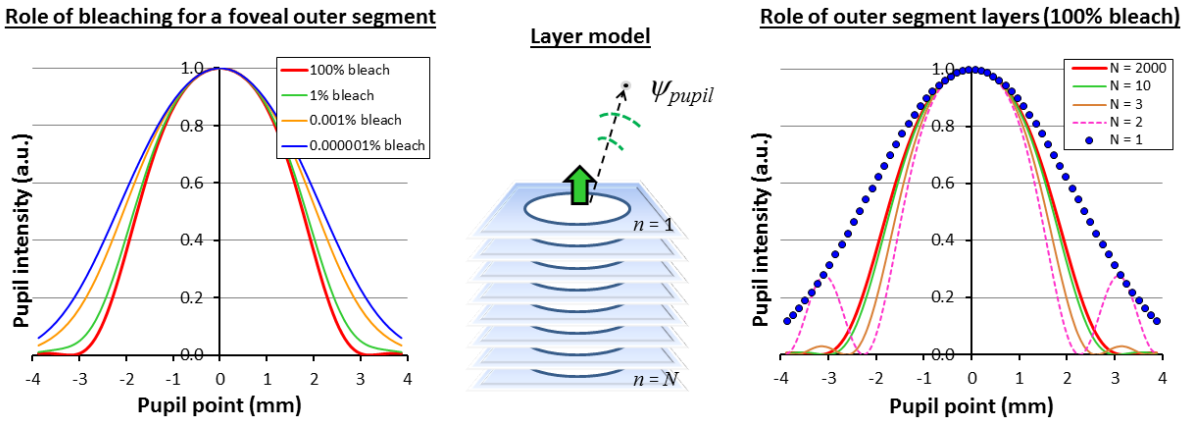

Fig. 20.13: SCE-I colour visibility function (left) and SCE-II hue-shift function (right). Note that the latter has not been pre-compensated for the SCE-I which, if included, will raise the function. Reproduced with permission from Fig. 8 in Brian Vohnsen, *On the spectral relation between the first and second Stiles–Crawford effect*, J. Mod. Opt. **56** ©2009 Taylor & Francis.

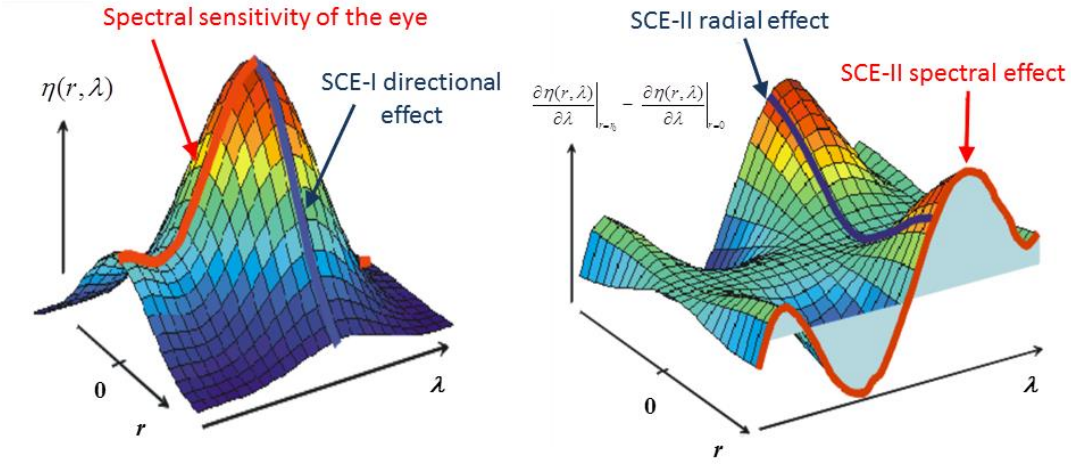

Fig. 20.14: Comparison of the standard Gaussian SCE-I function for two different directionality parameters (lines) with corresponding Airy disc functions (symbols) based on Eq. (13). Differences become only apparent near the pupil rim.

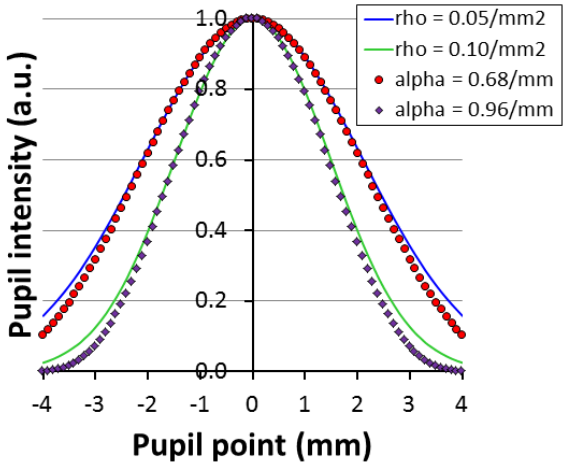

Fig. 20.15: The role of the SCE-I on the PSF and the MTF at 0.555μm wavelength for a schematic eye model with a large 8mm pupil without (green lines) and with (red lines) 0.1 dioptres defocus. The SCE-I ($\rho = 0.05/\text{mm}^2$ dashed line and $\rho = 0.10/\text{mm}^2$ dotted line) widens the PSF when compare the case of no SCE-I ($\rho = 0$ solid line) and dampens the off-axis intensity ringing which is particular apparent once defocus is introduced. Likewise, the SCE-I dampens the MTF at high frequencies while increasing the impact of low frequencies.

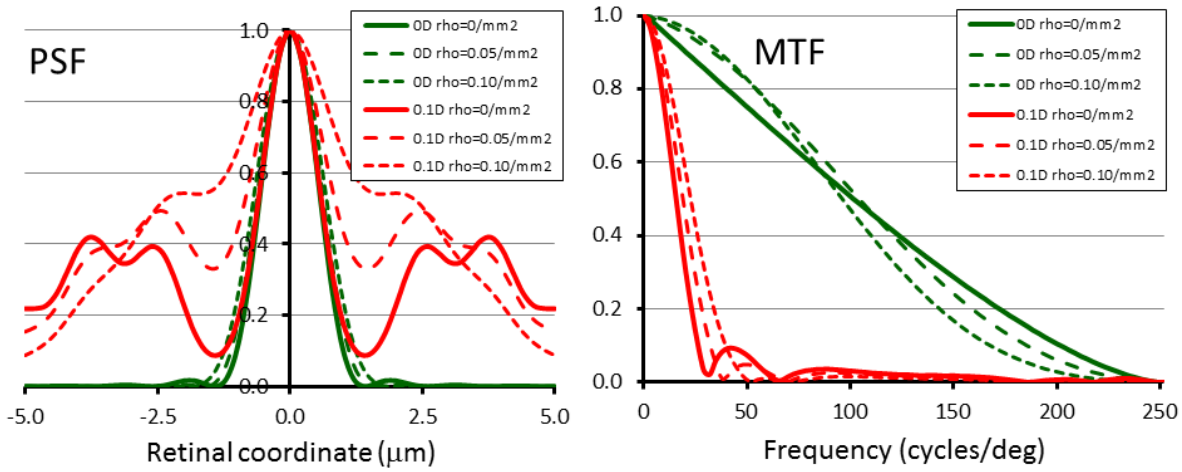

Fig. 20.16: Comparison of monochromatic PSF intensity images without (unguided) and with (effective) inclusion of the SCE-I as a retinal Gaussian waveguide mode with $w_m = 1.5\mu\text{m}$ that dampens the role of Zernike modes having even radial order away from the geometrical image point as shown here for defocus (left) and astigmatism (right), respectively.

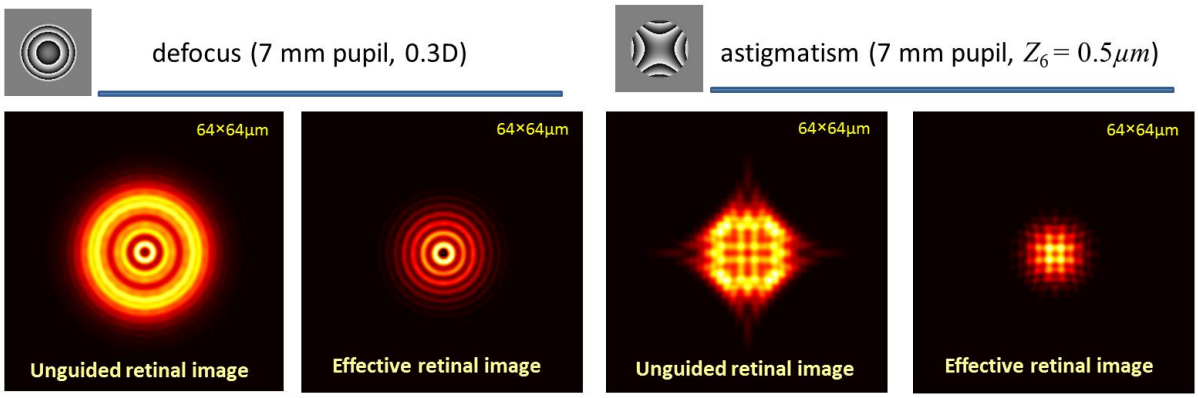

Fig. 20.17: Simulated scattering of light in a close-packed hexagonal arrangement of outer segments each with a 2µm diameter. Plane wave incidence on axis and 10° oblique (left) simulates SCE-I characterization with increased scattering into the interstitial matrix for oblique incidence. Simulating single-cone vision of a focused Gaussian beam (right) incident on a single or between two outer segments shows that light may enter neighbouring segments due to scattering. The figure has been reproduced with permission from Figs. 8 and 10 in Brian Vohnsen, *Directional sensitivity of the retina: A layered scattering model of outer-segment photoreceptor pigments*, Biomedical Optics Express **5** ©2014 Optical Society of America.

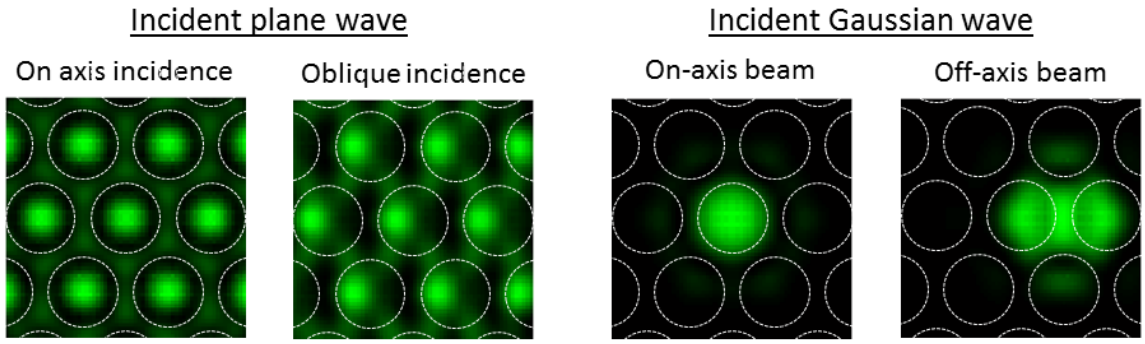

Fig. 20.18: Liquid-filled photonic-crystal fibre (LF-PCF). Castor-oil and temperature tuning is used to ensure waveguiding in a single-to-multimode regime in the individual densely-packed columns rather than in the core of the fibre whereby it resembles the parafoveal cone mosaic. Each column in the assembly has a 6.4µm diameter. Images show transmitted light though 30mm length of fibre with the incident being defocused and tightly focused, respectively, only a single column. HeNe lasers (543 and 633nm wavelength) have been used for the illumination.

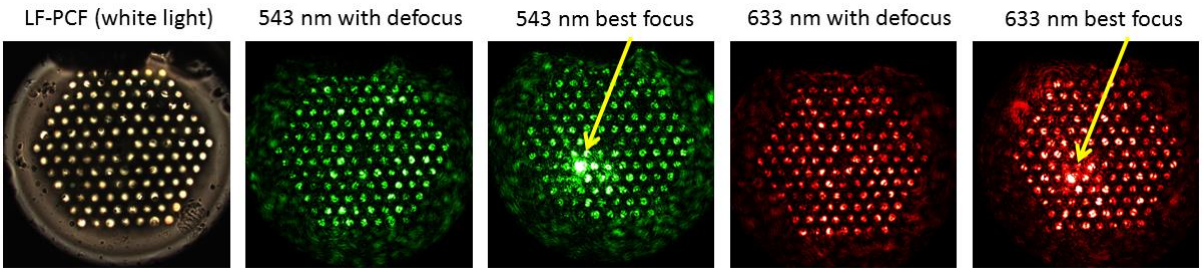

Fig. 20.19: Calculated flood-illumination retinal images for a schematic eye with 8mm pupil. The cone mosaic image of 82,000 cones/mm^2 (left) has been obtained from the backscattering of light for a hexagonal arrangement of 37 identical cones having 2.5μm diameter and three internal reflective layers (at the ellipsoid, at the inner-outer segment junction, and at the posterior end of the outer segment). The image shows the interference between light from different depths whereby a dark ring from destructive interference is produced at each. The same model has also been used to model a parafoveal rod-cone mosaic (right) showing details that resemble multimodal waveguides but are scattering patterns from the larger cones [122].

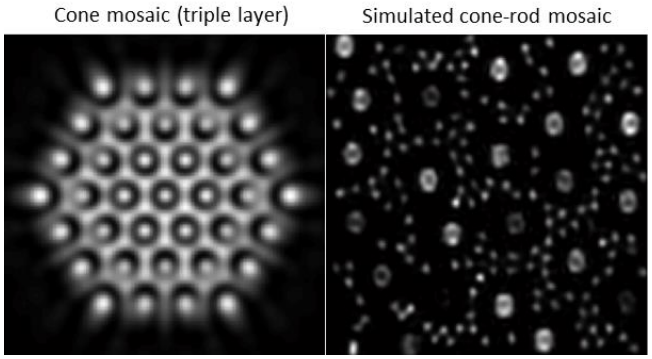

Table 20.1: Rotationally-symmetric visibility functions used to represent the SCE-I as a function of pupil point ($r = 0$ at the point of highest visibility).

Author(s)	SCE-I functions
Stiles [14]	$\eta(r) = 10^{-\rho r^2}$
Crawford [15]	$\eta(r) = e^{-\beta r^2}$
Moon and Spencer [96]	$\eta(r) = 1 - \beta r^2 + \gamma r^4$
Moon and Spencer [96]	$\eta(r) = (1-a) + a\cos(br)$
Enoch [52]	$\eta(r) = A(1+\cos Br)^2$
Rativa and Vohnsen [95]	$\eta(r) = a_1 10^{-\rho_1 r^2} + a_2 10^{-\rho_2 r^4} + a_3 10^{-\rho_3 r^6}$
Vohnsen [28]	$\eta(r) = \left(\frac{2J_1(\alpha r)}{\alpha r}\right)^2$